INFORMATION TO USERS

This manuscript has been reproduced from the microfilm master. UMI films the text directly from the original or copy submitted. Thus, some thesis and dissertation copies are in typewriter face, while others may be from any type of computer printer.

The quality of this reproduction is dependent upon the quality of the copy submitted. Broken or indistinct print, colored or poor quality illustrations and photographs, print bleedthrough, substandard margins, and improper alignment can adversely affect reproduction.

In the unlikely event that the author did not send UMI a complete manuscript and there are missing pages, these will be noted. Also, if unauthorized copyright material had to be removed, a note will indicate the deletion.

Oversize materials (e.g., maps, drawings, charts) are reproduced by sectioning the original, beginning at the upper left-hand corner and continuing from left to right in equal sections with small overlaps.

Photographs included in the original manuscript have been reproduced xerographically in this copy. Higher quality 6" x 9" black and white photographic prints are available for any photographs or illustrations appearing in this copy for an additional charge. Contact UMI directly to order.

Bell & Howell Information and Learning
300 North Zeeb Road, Ann Arbor, MI 48106-1346 USA
800-521-0600

UMI®

HARVARD UNIVERSITY
Graduate School of Arts and Sciences

THESIS ACCEPTANCE CERTIFICATE

The undersigned, appointed by the

Division

Department of Physics

Committee

have examined a thesis entitled "Multiscale Simulations of Indentation"

presented by Gregory Samuel Smith

candidate for the degree of Doctor of Philosophy and hereby certify that it is worthy of acceptance.

Signature ....

Typed name Efthimios Kaxiras, Chair

Signature Henry Ehrenreich

Typed name Henry Ehrenreich

Signature James R. Rice

Typed name James R. Rice

Date May 22, 2000

Multiscale Simulations of Indentation

A thesis presented
by

Greg Smith

to
The Department of Physics
in partial fulfillment of the requirements
for the degree of
Doctor of Philosophy
in the subject of

Physics

Harvard University
Cambridge, Massachusetts
June 2000

UMI Number: 9972435

Bell & Howell Information and Learning Company
300 North Zeeb Road
P.O. Box 1346
Ann Arbor, MI 48106-1346

Abstract

We simulate indentation of two technologically important materials, silicon, a prototypical covalent solid, and lead titanate ($PbTiO_3$), a prototypical piezoelectric material. Indentation experiments are an excellent probe of mechanical properties, but their interpretation is complicated by their multiscale nature. Indentation of silicon and $PbTiO_3$ in particular is complicated by the possibility of phase transformations occurring underneath the indenter. We describe our principal computational method, which is based on a finite element framework but uses atomistic potentials to determine the constitutive response of the system. Unlike traditional finite element methods, the nonlinear elastic effects, the symmetries of the underlying crystal, and the possibility of uniform structural phase transformations are naturally included in this formulation. Our simulations of silicon indentation reproduce experimental load vs. displacement curves and provide microscopic information such as the geometry of the region of phase transformed silicon. This information is linked to the macroscopic electrical resistance, providing a simple physical picture that gives a satisfactory explanation of experimental results. Our simulations of $PbTiO_3$ exhibit a number of surprising features, including a large asymmetry in the macroscopic load with the sign of the external electric field, continuous switching during indentation, and, under certain conditions, an inverted hysteresis loop in the load vs. displacement curve. We discuss the implications and predictions for experimental studies of piezoelectric materials.

Acknowledgements

I begin by thanking my advisor. Efthimios Kaxiras. His professional guidance and steady hand over several years of work was the constant that enabled me to finish. Prof. Kaxiras assembled a diverse and exciting research group. and being part of this group encouraged me take initiative and explore fields of science that I was completely unfamiliar with. Two members in particular stand out. Ellad Tadmor took me under his wing and gave me direction: Umesh Waghmare was always patient and knowledgeable, no matter what the topic. Both have become friends who I deeply respect. Both have moved on to other continents and are sorely missed. Beyond the Kaxiras group, I learned from a group of professors and fellow students at Harvard that is as intellectually generous as any I could hope to meet in the future.

But even with the support I had here at Harvard. scientific research has been very challenging for me. Some of my time here has been hard. and my family has been a constant source of support. and occasionally, when I wanted it least but needed it most, harsh honesty. I love you all.

So I write now the last paragraph of my thesis. and I'm thinking less about the thesis itself than about my time here as a graduate student. A lot has happened. To my friends. and to those I wish I knew better: to those who I love. and to those who I have loved: to those who have touched me. however briefly; to those who I talk to every day, and to those who I no longer talk to... thank you. Really I just haven't the words right now. I hope only that at some point in the past when I had the words. I said them to you. If not then I hope that I'll have the words in the future, and that I won't hesitate.

Citations to Previously Published Work

Chapters 2 and 4 are closely based on the following papers:

1. E. B. Tadmor, G. S. Smith, N. Bernstein and Efthimios Kaxiras, Phys. Rev. B **59**, 235 (1999).
2. G. S. Smith, E. B. Tadmor and Efthimios Kaxiras, Phys. Rev. Lett. **84**, 1260 (2000).

Contents

List of Figures

Chapter 1

Introduction

We begin with a simple hypothetical engineering problem. It illustrates the larger picture within which the investigation described in this thesis is embedded.

Suppose we want to build a better mouse trap. The better mouse trap requires a better spring. We could do a series of experiments to determine the spring geometry that optimally satisfies our various requirements. But initially we would prefer to do theoretical computational studies in order to better understand the physics of the system that can guide our trials. and to obtain detailed information difficult to obtain via experiment, such as the stress field throughout the spring. With a simple model and a few macroscopic constants that quantify the elastic characteristics and the yield threshold of the material, a wide range of information about the behavior of the spring can be obtained from simulations and theoretical work.

These sorts of models treat the spring as a continuous, homogeneous medium. But on the microscopic level it is made up of of grains composed of atoms arranged on a lattice that is full of defects, voids, and other features. The important point is that to determine many of the macroscopic behaviors of the spring, the atomic details of the spring are irrelevant. The length scale of the spring is on the order of meters (a big mouse trap), which is 10 orders of magnitude larger than the typical atomic spacing, and at least several orders of magnitude larger than other features–such as defects and grain boundaries–in the material. From the macroscopic viewpoint, the spring can be considered a continuous medium, with each point of the spring corresponding to a chunk of many, many atoms (and defects) that is statistically equivalent to every other chunk in the material. Certainly, the microscopic details are crucial for they ultimately determine all the properties of the spring, but all the relevant microscopic information is encoded in the values of the macroscopic constants.

But now suppose that we want to know how the behavior of the spring changes if we replace every tenth atom in the spring with an atom of a different element. The model we use will not change, but it is possible that the macroscopic constants will. Of course, we could test the new material in order to empirically determine how the values of the constants have changed. But could we do it without experimental input? In general it would be very difficult. Replacing some of the atoms in the material could change a variety of microscopic features, such as the bonding between atoms, or the ease with which defects can move. The changes in these microscopic details could affect the behavior of larger scale features, dislocation patterns or grain boundaries. These changes in turn affect larger scale features and their behavior and interactions, and so on until we reach the macroscopic scale. By that time, after being faced with a number of structures at a number of different length scales all interacting and affected by one another, predicting how the atomic substitutions affect the macroscopic constants is clearly very difficult indeed.

1.1 Multiscale Modelling

Seeking to understand how the macroscopic elastic and plastic properties of a spring are affected by atomic substitutions is an example of problem that might be explored in the field of multiscale modelling. Determining the scope of multiscale modelling is somewhat difficult. Perhaps this is because it is a field not defined so much by the computational or theoretical tools employed, or by the types of physical systems examined. but by its ultimate goal: to be able to understand how features and behaviors on all length and time scales–starting with the microscopic–interact and cause behavior observed on the macroscopic level. This is to say the least. an extremely ambitious goal, and likely will never be achieved for a general system. But already advances in methodology have been achieved. and strong collaborations have developed among engineers, physicists, chemists. materials scientists. and biologists. A number of groups are seeking to combine the strengths of different computational and theoretical methods in order to minimize weaknesses of the methods when isolated. and expand the range of length and time scales over which the methods can be used.

Given that the types of problems explored in the field of multiscale modelling are so difficult, a reasonable question would be: why bother? After all, in our example of the spring it would be easy to empirically determine the macroscopic constants after the atomic substitutions were made.

Making connections acros this hierarchy from microscopic to macroscopic is compelling for several reasons. First, it is a fascinating, endlessly complex issue. Curiosity is compelling in its own right. Even "simple" problems, such as why a paper clip breaks after repeated bendings. are incompletely understood. And in whatever problem one chooses to study, no matter how focused or esoteric. there is a limitless supply of surprises in the details, which may contribute to the fundamental understanding of the system of study and others like it. Investigation ends not because the mystery is exhausted, but because time has run out, or other issues are more pressing. This thesis is an appropriate illustration.

On a more practical level, a more fundamental understanding of the connection between microscopic and macroscopic would aid in the design of new materials. Technological advances have both opened doors to the creation of new materials, and created demand for materials with specific properties. Historically, creating useful new materials has been an art guided by experience. To develop a material with specific properties, countless different mixtures of constituents, different processing methods, etc., are tried in an effort achieve the balance of properties sought. Though experience and a vast base of knowledge help guide this time-consuming process, chance rules, since even the smallest changes in constituents or processing technique could substantially change the bonding or defect structure, which in turn affects the macroscopic properties. A better understanding of how changes in composition, for example, affect the atomic structure and defect population in a material, and how these microscopic properties affect macroscopic ones, would reduce the hand of chance in the process. Moreover, if the connection between microscopic and macroscopic is understood well enough so that all or part of the process could be done on a computer, valuable time, money, and materials could be saved.

Finally, recent advances in nanotechnology have demanded that the influence of microscopic structures be understood from square one. The knowledge gained over decades about new materials on the macroscopic scale does not necessarily transfer to the nanoscale. Nanoscale devices, which are devices whose size is on the order of microns or smaller, use different materials (silicon in particular is popular in nanosystems) and different fabrication techniques. Also, their small size directly or indirectly changes the physics that underlies their behavior. The small volumes of the devices means that a small number of defects can drastically influence its properties. Also, surfaces are much more important in nanosystems than in macroscopic systems since the surface area to volume ratio is much larger: reconstructions, surface impurities, and nicks or scratches take on heightened importance. Finally, the strains and stresses felt by the constituents can be much larger than in a macroscopic system.

1.2 Methodology

As our primary tool we use a version of the quasicontinuum method, a successful multiscale technique used to simulate solids developed by Tadmor *et al.* [5]. In its original form the quasicontinuum method uses a continuum formulation where deformations vary slowly over the scale of the atomic spacing (this is designated the "local" regime), and keeps track of the atomic degrees of freedom explicitly where displacements vary substantially on the atomic scale (this is the "nonlocal" regime). For example, in the quasicontinuum method the core of a dislocation would essentially be treated atomistically, while the atoms further away would be treated as part of a continuum.

The original formulation of the quasicontinuum methods could only model simple crystals. In order to explore some of technologically important materials that have multiple atoms per unit cell, we have extended the local version of the quasicontinuum method to handle complex Bravais crystals (we refer to this method subsequently as the QCBC method) [6]. The details of this extension are given in Chap. 2, but in the end we obtain a finite element method whose constitutive relation is not based on phenomenology, but is calculated from an appropriate atomic energy functional. This naturally incorporates the anisotropy and symmetries of the material, the nonlinearities associated with finite deformation, and the possible occurrence of uniform structural phase transformations.

This method is fairly specific, and rather stripped down compared to other multiscale computational methods. However, there are a range of systems that could benefit from analysis using this tool. Particularly powerful is the QCBC method's natural inclusion of nonlinear elastic effects and possible phase transformations within a finite element method that can accurately track stress fields in large systems. In many systems much larger than the atomic scale nonlinear elastic effects and phase transformations play a crucial role.

For example, in the emerging field of nanotechnology large internal stresses must be considered during fabrication of silicon structures [7]. Also, experimental work on silicon indentation indicates that phase transformations occur underneath the indenter and give rise to surprising macroscopic behavior [1, 2, 3, 8, 9, 10, 11, 12]. As another example, piezoelectric materials exhibit spontaneous polarization in a direction that can be switched by the application of external electric field or stress [13]. Nonlinear elastic effects and/or phase transformations (switching) are important in a variety of applications of these materials. Cao and Evans began their experimental exploration on the nonlinearity of piezoelectrics by noting that piezoelectric materials are used in actuators and sensors, and that "Many advanced applications require either large actuator displacements or large forces. Such conditions may cause nonlinearity, as well as permanent deformation..." [14]. Piezoelectrics are also used to make nonvolatile ferroelectric random-access memories, which take advantage of the switchable permanent polarization of piezoelectrics to ensure that binary information in a computer is retained even if the power is cut [15]. Finally, other possible applications include exploring the irreversible strain in steel that results from thermal cycling [16], and the martensitic transformation of NiAl in the vicinity of a crack tip [17, 18].

1.3 Intent

In this thesis we describe simulations using the QCBC method to model indentation of silicon and lead titanate ($PbTiO_3$).

We choose to focus on silicon and $PbTiO_3$ because these materials are crucial components in emerging technologies, and because there is experimental and theoretical work on these materials that we can use to guide the direction of our inquiry. Also, studying the two together is interesting because they are so different from one another on the microscopic level. Silicon is a prototypical covalently bound solid with a two atom unit cell, and $PbTiO_3$ is a prototypical piezoelectric that has a five atom unit cell with three different species. Examining both will test the range of our simulation technique and perhaps permit enlightening comparisons.

We focus on indentation for several reasons. First, in general indentation has proven to be an enormously successful experimental technique for measuring the mechanical properties of systems. Increasingly, it is being used to probe the properties of small volumes of materials. It is already widely used, for example, to measure the moduli and hardness of thin films [19, 20]. Second, indentation is an appropriate arena within which to explore the usefulness of our methodology. The large and inhomogeneous stress fields make an accurate representation of the microscopic energy surface of the indented material important, but at the same time the systems size is much larger than the atomic scale: in other words there are disparate length scales to contend with.

Finally, there is substantial experimental information on indentation of silicon and $PbTiO_3$. Indentation of silicon continues to be the focus of significant experimental work, sparked by the observation by Clarke *et al.* of evidence for a reversible phase transformation to a metallic phase of silicon underneath the indenter[8]. Subsequent work [1, 2, 3, 9, 10, 11, 12] has reinforced this hypothesis and produced intriguing macroscopic measurements, such as load vs. displacement curves or load vs. electrical resistance curves that exhibit hysteresis loops or discontinuities. Experimental work on piezoelectric indentation is more sparse, though indentation has been used to probe piezoelectric thin films in MEMS [21]. Ramamurty *et al.* performed a careful indentation study of certain piezoelectrics, but confined themselves to the linear regime [4].

This available experimental data is very important to our study. In the field of multiscale modelling, many of the simulation techniques are in their infancy and extremely complicated. Also, the types of physical systems studied are very complex, and it is difficult to extract information via experiment that can be directly compared with a simulated result. Compared to other multiscale methods, the QCBC method is fairly simple, and significant approximations (discussed in detail in Chap. 2) are made. But our principal intent is to include what we believe is the essential physics of the indented systems we seek to study: the rapidly varying strain fields caused by the indenter, strong elastic coupling between neighboring regions of the material, and a local energy surface that broadly captures the complexity of the true local energy surface (permitting, for example, structural phase transformations to occur). We aim to obtain a broad, though qualitative portrait of the microscopic and macroscopic behavior of the systems, and to make comparison with experiment in order to validate and understand the limitations of our method.

However, we are not content simply to try to reproduce experimental curves. We hope to contribute to the understanding of the systems we study, for certainly there is a need. Experiments by themselves have not been able to disentangle what is happening underneath the indenter, and theoretical and computational studies have been frustrated by the multiscale nature of the systems. Computational studies of silicon indentation, using either atomistic or continuum techniques, have not been able to reproduce even qualitatively the hysteretic effects or discontinuities observed in the experimental macroscopic curves [22, 23, 24, 25]. Theoretical studies of piezoelectric indentation are confined to the linear regime [26].

We seek to compare our simulation results with experiment, but also to understand why the experiments behave as they do. In addition we would like to obtain information difficult or impossible to obtain via experiment. Finally, we keep our eyes peeled for any behavior that, though not immediately experimentally relevant, is linked to curious or surprising physics.

Chapter 2

Extending the Local Quasicontinuum Method

The local version of the quasicontinuum method serves as our basic computational tool [5]. In this approach a continuum finite element formulation is used to characterize the mechanical response of a given system. The difference from standard finite element methodologies is that the constitutive response of the system is obtained from an atomistic calculation rather than an empirical phenomenological rule. The basic idea is that every point in a continuum corresponds to a very large region on the atomic scale. Thus, the constitutive response at that point, i.e. the stress-strain relation there, may be obtained by deforming the underlying crystal structure by the local strain to obtain the local state of stress. This is the local approximation of the quasicontinuum method. This approximation will be adequate as long as the variation of the continuum fields is "slow" on the atomic scale. When this breaks down, such as near defect cores, the nonlocal limit of the quasicontinuum method much be used, where the explicit positions of the atoms are taken into account [5]. Here we will focus entirely on the local version of the quasicontinuum method.

In its original version the quasicontinuum method was formulated with simple

Bravais crystals in mind. Many useful materials (silicon and piezoelectric materials being two examples) have more than one atom per primitive unit cell. Extending the quasicontinuum method to simulate materials with multiple atoms in a unit cell results in a method that maintains the advantages of traditional finite element methods, including correct treatment of the far field boundary conditions, and at the same time naturally incorporates the anisotropy and symmetries of the material, the nonlinearities associated with finite deformation, and the possible occurrence of uniform structural phase transformations. Finally, the efficiency of the finite element formulation permits computationally expensive atomistic energy functionals to be applied to significantly larger systems than would otherwise be possible.

2.1 Continuum Formulation

The continuum formulation adopted here is that of finite deformation. Thus, no assumptions are made regarding the smallness of the strains. Within a finite deformation framework we differentiate between a solid in its reference or undistorted state (also referred to as the *material* frame) and its current or deformed state (called the *spatial* frame). Consider a crystal occupying a configuration B_0 in the reference frame which is mapped to its current shape B by the deformation mapping $\boldsymbol{\phi}(\mathbf{X})$ (see figure 2.1). Thus every point $\mathbf{X}$ in the reference configuration is mapped to some point $\mathbf{x}$ in the current configuration by

$$\mathbf{x} = \boldsymbol{\phi}(\mathbf{X}) = \mathbf{X} + \mathbf{u}(\mathbf{X}), \tag{2.1}$$

where $\mathbf{u}(\mathbf{X})$ is the displacement at point $\mathbf{X}$. The deformation of an infinitesimal neighborhood of point $\mathbf{X}$ (represented as a shaded circle in the figure) is completely characterized by the linear part of $\boldsymbol{\phi}(\mathbf{X})$. This defines an affine mapping,

$$d\mathbf{x} = \mathbf{F}d\mathbf{X}, \tag{2.2}$$

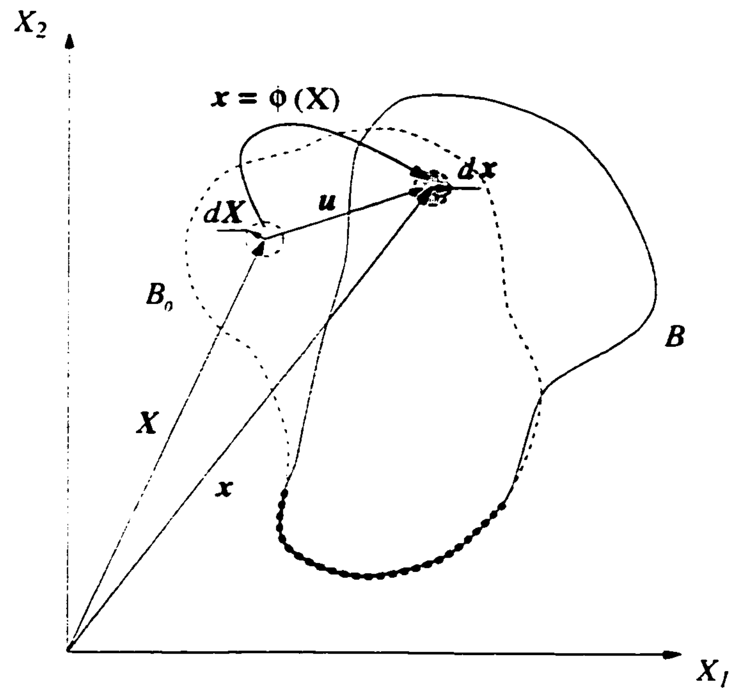

Figure 2.1: The deformation mapping relating the material (B_0) and spatial (B) configurations. Displacements are specified on the dark dashed part of the boundary (∂B_{0U}) and tractions on the remaining boundary (∂B_{0T}).

where $\mathbf{F}$ is the deformation gradient.

$$\mathbf{F} = \nabla_0 \boldsymbol{\phi} = \frac{\partial \boldsymbol{\phi}}{\partial \mathbf{X}} = \mathbf{I} + \frac{\partial \mathbf{u}}{\partial \mathbf{X}}, \tag{2.3}$$

where $\mathbf{I}$ is the identity tensor. In indicial notation, $F_{iJ} = \phi_{i,J}$ and $dx_i = F_{iJ} dX_J$ where upper case indices refer to the material frame, lower case indices to the spatial frame, $(\cdot)_{,J}$ indicates differentiation with respect to X_J and Einstein's summation convention on repeating indices is observed.

The deformation mapping and its gradient characterize the kinematics of the deformation. The constitutive nature of the material is introduced through the strain energy density function W which relates the energy at a point to the local state of the material. In general W will depend on the deformation field, internal variable fields, the temperature field, external fields such as an electric field, etc. We will include the effect

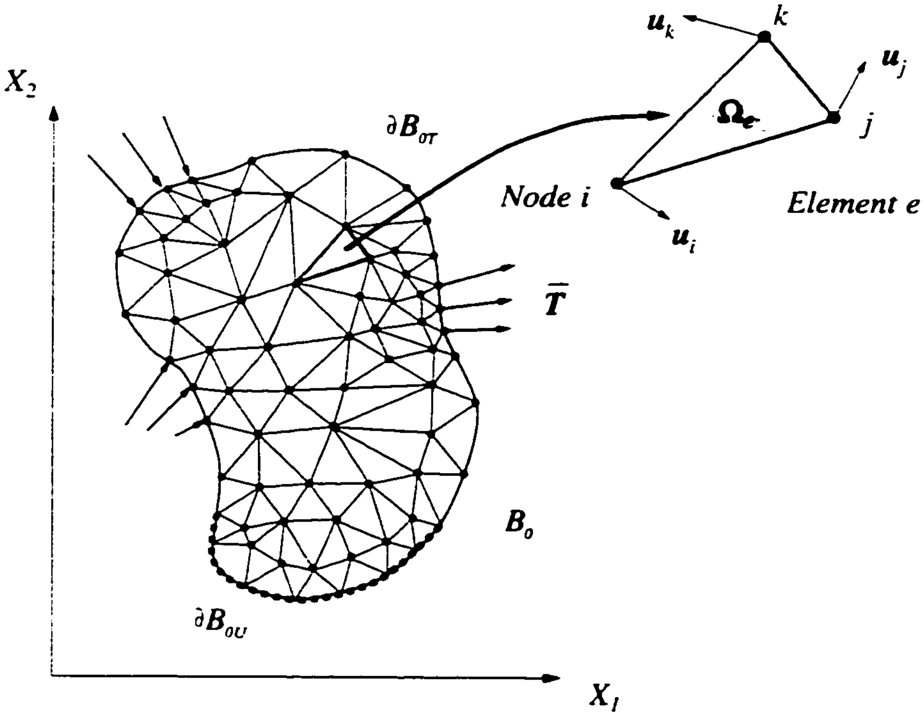

Figure 2.2: Finite element mesh of reference solid B_0 showing boundary conditions and nodal degrees of freedom.

of the temperature and external fields only for $PbTiO_3$, and then only in a simple way at the atomic level (see Sec. 2.3.3 for more details). Also, when we later introduce the connection with an underlying complex Bravais lattice, we find the deformation gradient alone is not sufficient to determine the state of the system. Essentially we have introduced internal variables, and we consider this complication in Sec. 2.2.

So for now at each point in the material we consider W to be a function of the deformation gradient and its derivatives. From the hypothesis of locality and use of the entropy production inequality it may be shown [27] that W can only be a function of $\mathbf{F}$, i.e. $W = W(\mathbf{F})$ and not its derivatives or any other variables. Furthermore, by invoking the postulate of material frame indifference it can also be shown [27] that the dependence of W on F can only be through the right Cauchy-Green tensor $\mathbf{C} = \mathbf{F}^T\mathbf{F}$. This is simply stating that the energy of the system as a whole is invariant with respect to rigid body rotations. However, for the current formulation it is more convenient to work in terms of $\mathbf{F}$ instead of $\mathbf{C}$.

We may now formulate the general boundary value problem. To this end, we partition the reference boundary ∂B_0 into a displacement component ∂B_{0U} and a traction component ∂B_{0T} (see Fig. 2.1). The solid is subjected to prescribed displacements $\overline{\mathbf{u}}$ on ∂B_{0U} and prescribed tractions $\overline{\mathbf{T}}$ on ∂B_{0T}. Stable configurations of the crystal are identified with minimizers of the potential energy,

$$\Pi = \inf_{\mathbf{u}} \left\{ \int_{B_0} W(\mathbf{F}) dV_0 - \int_{\partial B_{0T}} \left(\overline{\mathbf{T}} \cdot \mathbf{u} \right) dS_0 \right\}, \tag{2.4}$$

where $\mathbf{F}$ is a function of $\mathbf{u}$ through (2.3), and the trial deformations $\mathbf{u}$ satisfy the essential boundary condition $\mathbf{u} = \overline{\mathbf{u}}$ on ∂B_{0U}.

To solve the problem we discretize our continuum into a set of finite elements bounded by nodes (see Fig. 2.2.) The continuous displacement field $\mathbf{u}$ is now approximated by finite element interpolation from its nodal values $\mathbf{u}_a$,

$$\mathbf{u}(\mathbf{X}) \simeq \tilde{\mathbf{u}}(\mathbf{X}) = \sum_{a=1}^{N_n} \mathbf{u}_a N_a(\mathbf{X}), \tag{2.5}$$

where there are N_n nodes in the mesh and $N_a(\mathbf{X})$ are the standard finite element interpolation, or 'shape' functions [28]. The potential energy in Eq. 2.4 may also be rewritten in discretized form,

$$\tilde{\Pi}(\{\mathbf{u}_i\}) = \sum_{e=1}^{N_e} \int_{\Omega_e} W(\mathbf{F}) dV_0 - \sum_{a=1}^{N_n} \int_{\partial B_{0T}} \left(\overline{\mathbf{T}} \cdot \mathbf{u}_a \right) N_a dS_0, \tag{2.6}$$

where N_e is the number of elements and Ω_e is the volume of element e. In our formulations all integrals in Eq. 2.6 are carried out by numerical quadrature with a single quadrature point [28],

$$\int_{\Omega_e} W(\mathbf{F}) dV_0 \approx \Omega_e \hat{W}(\mathbf{F}_e), \tag{2.7}$$

where $\mathbf{F}_e$ is the constant deformation gradient in the element.

To find the equilibrium configuration we need to minimize the potential energy $\tilde{\Pi}(\{\mathbf{u}_i\})$ in Eq. 2.6. We use a conjugate gradient algorithm (see Ref. [29] for more details) which requires the gradient of $\tilde{\Pi}$ with respect to $\mathbf{u}_a$. Differentiating Eq. 2.6 we have

$$\frac{\partial \tilde{\Pi}}{\partial u_{ai}} = \sum_{e=1}^{N_e} \int_{\Omega_e} P_{iJ} N_{a,J} dV_0 - \int_{\partial B_{0T}} \overline{T}_i N_a dS_0. \tag{2.8}$$

where $\mathbf{P}$ is the first Piola-Kirchhoff stress tensor defined by

$$P_{iJ} = \frac{\partial W}{\partial F_{iJ}}. \tag{2.9}$$

Note that the first Piola-Kirchhoff stress is a mixed tensor, i.e. it has one index in the reference configuration and one in the spatial configuration and it is not symmetric.

2.2 Connection to the Atomistic Potential

In order to formulate a constitutive law for a continuum from the atomic interactions of the discrete crystal that underlies it, we must hypothesize a connection between the continuum displacement field and the motion of atoms. The standard reasoning consistent with the locality approximation of continuum mechanics is that the atomic environment at a continuum point is characterized by the deformation gradient there; this is referred to as the Cauchy-Born hypothesis [30]. Thus, each continuum point is taken to represent a large, essentially infinite, region on the atomic scale which is homogeneously distorted according to the deformation gradient at the point. The energy of the distorted crystal and its derivatives can then be obtained from any atomistic model of choice from approximate classical descriptions to rigorous first principles methods through the use of periodic boundary conditions.

It is worth noting the limitations of the local approximation. First, a local formulation has no internal length scale, thus it is the strain in an element and not its absolute size that enters into the constitutive calculation. This approximation will be valid as long as the continuum displacement field is slowly varying on the atomic scale. If it is not, a nonlocal formulation will be necessary (see Ref. [31] for details).

Second, surfaces and interfaces between different phases or in a polycrystal will be invisible to a local formulation. It *is* possible within a local formulation to include regions with different constitutive descriptions, and of course in a numerical simulation the model is finite and must terminate at surfaces. However, the energetics of the interfaces will not be accounted for since, as stated, the constitutive calculations at each point are performed for an infinite crystal free of boundaries. This introduces another minimum length scale below which the simulation method is not valid. Take the example of two phases in two adjacent finite elements. In general, if the interface energy between two phases is comparable to or larger than the typical change in volume energy due to a phase transformation, then ignoring the interface energy will not capture the correct energetics of the system. If the interface energy per unit area is ϵ_I, and the bulk energy difference between phases per unit volume is estimated with ϵ_V, then equating energies gives a length scale

$$l_\circ = \epsilon_I / \epsilon_V. \tag{2.10}$$

For the local quasicontinuum quasicontinuum method to be valid, it must be used to model systems such that the finite elements have dimension $l \gg l_\circ$ [1].

---

[1] For the applications to silicon and $PbTiO_3$, this inequality is satisfied. For silicon, from density func-

Third, cracks and atomic scale defects such as vacancies or dislocations are not included in the simulation. The method uses an infinite, perfect crystal to calculate energies: there are no defects or cracks in the reference crystal, nor is there a mechanism for introducing them as the simulation proceeds. Also, the topology of the finite element mesh is fixed. Finite elements cannot separate from one another in order to simulate crack growth.

Now let us consider the application of the Cauchy-Born rule to complex Bravais lattices. We consider a crystal which may be represented as a Bravais lattice with Bravais vectors $\mathbf{A}_k$ (k=1,3) and $N_a + 1$ basis atoms per Bravais site. The coordinates of the atoms making up the lattice in the reference coordinate system are

$$\mathbf{X}^{\nu} = \ell_k^N \mathbf{A}_k + \mathbf{b}^n, \tag{2.11}$$

where N is the Bravais site number running from 0 to N_s (there are $N_s + 1$ sites and 0 corresponds to the origin site where $\ell_k^0 = 0$), n is an index referring to the basis atom number, $\boldsymbol{\ell}^N$ is a triplet of integers locating Bravais site N in space and $\mathbf{b}^n$ is the position of basis atom n relative to the Bravais site. In order to simplify the notation we bundle the site and basis atom number into a single index denoted by a Greek letter, e.g. $\nu = (N, n)$, which completely identifies an atom. Without loss of generality, we may set $\mathbf{b}^0 = 0$ so that one basis atom always lies at the Bravais site. Applying the Cauchy-Born rule, the positions of the atoms after deformation is given by,

$$\begin{aligned} \mathbf{x}^{\nu} &= \mathbf{F}\left(\mathbf{X}^{\nu} + \boldsymbol{\zeta}^n\right), \\ &= \mathbf{F}\left(\ell_k^N \mathbf{A}_k + \mathbf{b}^n + \boldsymbol{\zeta}^n\right), \end{aligned} \tag{2.12}$$

where $\boldsymbol{\zeta}^n$ are additional inner displacements resulting from energy relaxation with respect to the basis atom positions (see Refs. [32, 33, 34] for details). Again, without loss of

---

tional theory calculations of the interface energy between diamond silicon and β-Sn, we estimate the length scale to be on the order of 10 nm, two orders of magnitude smaller than the minimum finite element size in the silicon indentation simulations in Chap. 4. The length scale in the simulations is set by comparing with the relevant features of experimental setups. For $PbTiO_3$, comparison is with experimental systems that are two orders of magnitude larger than the silicon experimental systems, ensuring that the inequality is satisfied.

generality and in order to rule out rigid body translation we may fix the lattice by setting $\zeta^0 = 0$. By defining the inner displacements ζ^n in the reference configuration we automatically guarantee the invariance of these measures with respect to rigid body rotation [32].

In general, the energy of a collection of atoms $\{\mathbf{x}^\nu\}$ will be a function of their coordinates,

$$E = E(\{\mathbf{x}^\nu\}). \tag{2.13}$$

The strain energy density W follows by normalizing this quantity with respect to the atomic volume in the reference configuration Ω,

$$W = \frac{1}{\Omega} E(\{\mathbf{x}^\nu\}). \tag{2.14}$$

We stated earlier that the strain energy function must obey material frame indifference, i.e. invariance with respect to rigid body rotation. Martin [33] studied the implication of this to atomic energy functions and concluded that the energy can only depend on the atomic coordinates through scalar products of their relative positions. We define $\mathbf{R}$ and $\mathbf{r}$ as relative position vectors between pairs of atoms in the reference and deformed configurations, respectively,

$$\begin{aligned} \mathbf{R}^{\nu\mu} &= \mathbf{X}^\mu - \mathbf{X}^\nu, \\ &= \left(\ell_k^M - \ell_k^N\right) \mathbf{A}_k + \mathbf{b}^m - \mathbf{b}^n, \end{aligned} \tag{2.15}$$

and

$$\begin{aligned} \mathbf{r}^{\nu\mu} &= \mathbf{x}^\mu - \mathbf{x}^\nu \\ &= \mathbf{F}\left[\left(\ell_k^M - \ell_k^N\right) \mathbf{A}_k + \mathbf{b}^m - \mathbf{b}^n + \zeta^m - \zeta^n\right], \end{aligned} \tag{2.16}$$

where $\mu = (M, m)$ and $\nu = (n, n)$. From (2.16) it is clear that scalar dot products of $\mathbf{r}$ will depend on $\mathbf{F}$ through $\mathbf{F}^T\mathbf{F}$ or $\mathbf{C}$ as expected from material frame indifference. Moreover, we can see from Eq. 2.16 that $\mathbf{r}$ is a function of the atomic positions in the reference coordinate system, which do not change, the deformation gradient, **F**, and the inner displacements, ζ^n. So in general, we have $W = W(\mathbf{F}, \boldsymbol{\zeta}^1, \cdots, \boldsymbol{\zeta}^{N_a})$.

Here the deformation gradient **F** is not sufficient to completely determine the state of the system, and we must postulate how to determine the values of the internal variables. The simplest condition that is physically reasonable and consistent with the local approximation of the quasicontinuum method is to require that for a given macroscopic deformation, the strain energy be minimized with respect to the inner displacements [34]:

$$\left.\frac{\partial W}{\partial \boldsymbol{\zeta}^n}\right|_{\mathbf{F}} = 0, \qquad n = 1, \ldots, N_a, \tag{2.17}$$

and $\partial^2 W / \partial \boldsymbol{\zeta}^m \partial \boldsymbol{\zeta}^n$ must be positive definite. It is minimizing the strain energy with respect the inner displacements that enables this method to naturally permit uniform phase transformations to occur. As the deformation gradient becomes sufficiently large, the positions of the internal displacements may go unstable and the minimization process will cause them to move to a nearby local minimum in the energy surface. In practical experience, this movement of the inner displacements to another local minima almost always corresponds to a change in structure of the crystal.

The relations in Eq. 2.17 form a system of $3N_a$ equations for the $3N_a$ unknowns ζ^n_j. The dependence of W on $\boldsymbol{\zeta}^n$ will generally be highly complex and the resulting system of equations coupled and nonlinear. Practically, the solution of Eq. 2.17 is best achieved by employing a numerical minimization algorithm, such as the conjugate gradient method, to minimize W with respect to the inner displacements with the deformation gradient **F** held fixed. This minimization can be strongly history dependent at zero temperature (i.e. the local minimum to which it converged will depend on the initial guess). Thus, it is necessary to store the inner displacements $\boldsymbol{\zeta}^n$ for each finite element, using the previous solution at that point as the initial guess for the next iteration.

After minimization, we obtain the equilibrium inner displacements $\hat{\boldsymbol{\zeta}}^n = \hat{\boldsymbol{\zeta}}^n(\mathbf{F})$, which implies that the strain energy is only a function of **F**,

$$W = W(\mathbf{F}, \hat{\boldsymbol{\zeta}}^n) = W(\mathbf{F}, \hat{\boldsymbol{\zeta}}^n(\mathbf{F})) \equiv \hat{W}(\mathbf{F}). \tag{2.18}$$

We may now compute the stress and moduli tensors in the presence of internal relaxation. The first Piola-Kirchhoff stress was defined earlier in Eq. 2.9. For a complex Bravais lattice we have,

$$P_{iJ} = \frac{\partial \hat{W}}{\partial F_{iJ}} = \left.\frac{\partial W}{\partial F_{iJ}}\right|_{\hat{\zeta}} + \left.\frac{\partial W}{\partial \hat{\zeta}^n_K}\right|_{\hat{\zeta}} \left.\frac{\partial \hat{\zeta}^n_K}{\partial F_{iJ}}\right|_{\hat{\zeta}}. \tag{2.19}$$

where the subscript $\hat{\zeta}$ indicates the expression is evaluated at the relaxed inner displacements $\hat{\zeta}^n$. Under ideal conditions the second term in Eq. 2.19 drops out due to Eq. 2.17 and we are left with the standard definition for the stress tensor evaluated at the relaxed inner displacements.

$$\mathbf{P} = \left.\frac{\partial W}{\partial \mathbf{F}}\right|_{\hat{\zeta}}. \tag{2.20}$$

In practical applications Eq. 2.17 is satisfied only approximately since a numerical procedure is used, but errors can be made sufficiently small by making sure that Eq. 2.17 satisfied to machine precision.

2.3 Interatomic Potentials

Up to this point the discussion has been without reference to a specific atomic energy functional. In an ideal world, we would use density functional theory (DFT) as the atomic energy functional. This method is based on quantum mechanics and over the past several decades has been an enormously successful tool for making quantitative predictions about the properties and behavior of a wide variety of materials [35, 36]. However, DFT is too computationally intensive to be used in the local quasicontinuum method, so we turn to alternative methods that calculate energies significantly faster than DFT, but are not as accurate.

We have implemented three potentials: an empirical potential for silicon developed by Stillinger and Weber [37], a tight-binding energy functional for silicon developed by Bernstein and Kaxiras [38], and an energy functional for $PbTiO_3$ developed by Waghmare and Rabe based on density functional theory [39]. Two potentials were implemented for silicon in an effort to understand how different potentials affect simulation results (discussed in Chap. 3). Implementing a potential requires determining the energy density, W in Eq. 2.14. Also, the derivative of W with respect to the internal degree of freedom must be determined in order to satisfy Eq. 2.17, and derivative of W with respect to the deformation gradient must be determined in order to calculate the Piola-Kirchoff stress, which is used in Eq. 2.8 to minimize the potential energy.

2.3.1 Empirical Potential for Silicon

The Stillinger-Weber potential has a simple form and is a function of atomic positions; no attempt is made to directly model the quantum mechanical behavior of the electrons. Eight adjustable parameters in the functional form were optimized to match a range of thermodynamic properties of silicon [37]. There is a two-body (V_2) and three-body (V_3) contribution to the energy,

$$E = \sum_{\eta} \left[\frac{1}{2} \sum_{\mu} V_2(r^{\eta\mu}) + \sum_{\mu<\nu} V_3(r^{\eta\mu}, r^{\eta\nu}, \cos\theta^{\eta\mu\nu}) \right], \tag{2.21}$$

where $r^{\eta\mu}$ is the distance between atoms η and μ and $\theta^{\eta\mu\nu}$ is the angle defined by the triplet of atoms η, μ and ν. In Eq. 2.21 a sum over a Greek index implies a double summation over the Bravais sites and basis atoms associated with the index. In this case the indices η, μ and ν run over all Bravais sites and associated basis atoms in the solid.

For a homogeneously distorted crystal, the same basis atoms at different lattice sites will experience identical environments and thus the calculation of (2.21) may be limited to a single unit cell in order to obtain the correct energy density. For convenience we choose to compute the energy with respect to the origin Bravais site $o = (0, a)$,

$$W = \frac{1}{\Omega} \widehat{\sum_{o}} \left[\frac{1}{2} \sum_{\mu} V_2(r^{o\mu}) + \sum_{\mu<\nu} V_3(r^{o\mu}, r^{o\nu}, \cos\theta^{o\mu\nu}) \right], \tag{2.22}$$

where Ω is the primitive Bravais cell volume, $r^{o\mu}$ is the distance of atom μ from basis atom a of the origin Bravais site and $\theta^{o\mu\nu}$ is the angle measured relative to that atom. The $\widehat{\sum}$

symbol indicates summation only over the second component of a Greek index (i.e. over a in this case).

Given the specific potential description of Eq. 2.22 we may explicitly obtain the derivatives of the strain energy density appearing in the expressions for the stress (Eq. 2.19). The first derivatives are given

$$\frac{\partial W}{\partial F_{iJ}} = \frac{1}{\Omega}\widetilde{\sum_{o}}\left\{\frac{1}{2}\sum_{\mu} V_{2,\mu}\frac{\partial r^{o\mu}}{\partial F_{iJ}} + \sum_{\mu<\nu}\left[V_{3,\mu}\frac{\partial r^{o\mu}}{\partial F_{iJ}} + V_{3,\nu}\frac{\partial r^{o\nu}}{\partial F_{iJ}} + V_{3,\theta}\frac{\partial \cos\theta^{o\mu\nu}}{\partial F_{iJ}}\right]\right\}, \quad (2.23)$$

$$\frac{\partial W}{\partial \zeta^{p}_{K}} = \frac{1}{\Omega}\widetilde{\sum_{o}}\left\{\frac{1}{2}\sum_{\mu} V_{2,\mu}\frac{\partial r^{o\mu}}{\partial \zeta^{p}_{K}} + \sum_{\mu<\nu}\left[V_{3,\mu}\frac{\partial r^{o\mu}}{\partial \zeta^{p}_{K}} + V_{3,\nu}\frac{\partial r^{o\nu}}{\partial \zeta^{p}_{K}} + V_{3,\theta}\frac{\partial \cos\theta^{o\mu\nu}}{\partial \zeta^{p}_{K}}\right]\right\}. \quad (2.24)$$

In the above expressions $(\cdot)_{,\mu}$ indicates differentiation with respect to $r^{o\mu}$ and $(\cdot)_{,\theta}$ indicates differentiation with respect to $\cos\theta^{o\mu\nu}$. The derivatives in Eq. 2.23 and Eq. 2.24 and the second derivatives contain partial derivatives of the form $\partial r/\partial \mathbf{F}$, $\partial r/\partial \zeta$, $\cdots$ These are kinematic identities and they are given in the appendix of Ref. [6].

2.3.2 Tight Binding Hamiltonian for Silicon

The tight binding approach is a very different way of modelling the interactions between atoms compared to the SW potential. In this method the atoms are treated as classical particles that interact in part through an effective potential exerted by the electrons that are treated quantum-mechanically. Hypothetical basis orbitals with the angular symmetries of single atom eigenstates are centered around each atom. The details of the basis functions do not enter into the energy calculation, but only the interactions between basis elements $|\phi_i\rangle$ that form the overlap matrix,

$$S_{ij} = \langle\phi_i|\phi_j\rangle\,, \quad (2.25)$$

and the Hamiltonian matrix,

$$H_{ij} = \langle\phi_i|H|\phi_j\rangle\,. \quad (2.26)$$

The indices i and j run over the all the atoms and all the basis elements centered on each atom. The energy eigenvalues are found by solving the generalized eigenvalue equation,

$$H_{ij}\psi_{nj} = \epsilon_n S_{ij}\psi_{nj}, \tag{2.27}$$

where ϵ_n is the nth eigenvalue and ψ_{nj} is the jth component of the nth eigenvector.

In the particular tight-binding model used here, the energy density, W, is made up of a classical two-body pair repulsion term and a band structure term [38].

$$W = \frac{1}{\Omega}\widehat{\sum_{o}}\left[\frac{1}{2}\sum_{\mu} V_2(r^{o\mu})\right] + \frac{2}{\Omega N_k}\sum f_n\epsilon_n, \tag{2.28}$$

where N_k is the number of k-points, and the sum $\sum_n$ is over both bands and k-points. The pair potential models the screened Coulomb repulsion of the atomic cores, while the quantum mechanical behavior of the valence electrons is modelled explicitly in the band structure term. The distribution f_n is taken to be the Fermi function.

$$f_n = \frac{1}{1 + e^{((\epsilon_n - \epsilon_f)/\sigma)}}, \tag{2.29}$$

where ϵ_f is the Fermi energy, and σ is a smoothing parameter. Eq. 2.29 is a convenient mathematical function that makes a smooth transition between the occupied ($f_n = 1$) and the unoccupied states ($f_n = 0$). The smoothing parameter σ is used to maintain numerical stability, particularly for metallic forms of silicon. It is not related to the physical temperature of the system.

Ideally simulation results should not depend on the value of σ. To that end, for the tight-binding "energy" we use an average of the energy and free energy density, denoted $\widetilde{W}$, which has an entropic term added to the expression in (2.28),

$$\widetilde{W} = W + \frac{\sigma}{\Omega N_k}\sum_n (f_n \ln(f_n) + (1 - f_n)\ln(1 - f_n)). \tag{2.30}$$

Our reason for using $\widetilde{W}$ rather than W is that while the energy and free energy density both vary as σ^2, the average of the two varies as σ^4 [40]. For our particular case we can verify this by assuming that we have a smooth, continuous density of states, $g(\epsilon)$

(this is to permit differentiation. which is required for our argument). Thus our starting expression for $\widetilde{W}$ is the same as the expression in (2.30), except that $(2/\Omega N_k)\sum_n$ is replaced by $\int g(\epsilon)d\epsilon$. We consider $\widetilde{W}$ to be a function of σ and ϵ_f, and require that the number of electrons, N, be independent of the smoothing parameter. Then.

$$\frac{d\widetilde{W}}{d\sigma} = \frac{\partial \widetilde{W}}{\partial \sigma} - \frac{\partial \widetilde{W}}{\partial \epsilon_f}\left(\frac{\partial N}{\partial \sigma} \Big/ \frac{\partial N}{\partial \epsilon_f}\right). \tag{2.31}$$

Determining the zero order σ contributions to the derivatives with respect to the Fermi energy is immediate. and additional terms in the expansion are of order σ^2.

$$\frac{\partial \widetilde{W}}{\partial \epsilon_f} = \epsilon_f g(\epsilon_f) + O(\sigma^2). \tag{2.32}$$

$$\frac{\partial N}{\partial \epsilon_f} = g(\epsilon_f) + O(\sigma^2). \tag{2.33}$$

The derivatives with respect to σ can be evaluated using Sommerfield's lemma [41],

$$\frac{\partial \widetilde{W}}{\partial \sigma} = \frac{\pi^2}{3}\epsilon_f g'(\epsilon_f)\sigma + O(\sigma^3), \tag{2.34}$$

$$\frac{\partial N}{\partial \sigma} = \frac{\pi^2}{3} g'(\epsilon_f)\sigma + O(\sigma^3). \tag{2.35}$$

Combining eqs. (2.31 - 2.35), we obtain,

$$\frac{d\widetilde{W}}{d\sigma} \approx O(\sigma^3). \tag{2.36}$$

Taking the derivative of the expansion of $\widetilde{W}$ with respect to atom positions confirms that the forces have the same smoothing parameter dependence as $\widetilde{W}$.

For the derivatives of $\widetilde{W}$,

$$\frac{\partial \widetilde{W}}{\partial F_{iJ}} = \frac{1}{\Omega}\widehat{\sum_o}\left[\frac{1}{2}\sum_\mu V_{2,\mu}\frac{\partial r^{o\mu}}{F_{iJ}}\right] + \frac{1}{\Omega N_k}\sum_n\left[2f_n - \frac{1}{\sigma}\hat{f}_n\left(\epsilon_n - \frac{\sum_m \epsilon_m \hat{f}_m}{\sum_m \hat{f}_m}\right)\right]\frac{\partial \epsilon_n}{\partial F_{iJ}}, \tag{2.37}$$

where

$$\hat{f}_n = \frac{e^{((\epsilon_n - \epsilon_f)/\sigma)}}{(1 + e^{((\epsilon_n - \epsilon_f)/\sigma)})^2}. \tag{2.38}$$

With the aid of the Hellman-Feynman theorem [42, 43] one can show,

$$\frac{\partial \epsilon_n}{\partial F_{iJ}} = \frac{1}{2}\widehat{\sum_o}\sum_\mu\left[\sum_{lm}\psi^*_{nl}\left(\frac{\partial H_{lm}}{\partial r_i^{o\mu}} - \epsilon^n\frac{\partial S_{lm}}{\partial r_i^{o\mu}}\right) r_k^{o\mu}\psi_{nm}\right] F_{Jk}^{-1}, \tag{2.39}$$

where $r_i^{o\mu}$ is the ith component of the the position vector between the atoms o and μ.

There are additional practical considerations that must also be considered when using a quantum mechanical Hamiltonian within the quasicontinuum method. In the course of a simulation where a nonuniform load is applied, all spatial symmetries of the cubic silicon unit cell may be broken. As a result, no special k-points can be used. Furthermore, extreme deformations may occur in some elements, and the band gap of silicon may disappear, effectively making the silicon a metal. To maintain numerical stability, either a very dense k-point mesh, or a very large smoothing parameter σ (see Eq. 2.29) must be used. Using a very dense k-point mesh without special k-points would be computationally prohibitive; using a very large smoothing parameter, even when mixing the energy and free energy (see Eq. 2.30), would give unphysical energies and forces that depend on σ.

After much trial and error we settled on a middle ground that gave converged results and enabled semi-conductor silicon to transform to a metallic phase in the course of a simulation while maintaining numerical stability. We used a 5x5x5 k-point grid, which corresponds to 63 k-points (time reversal symmetry is intact since there is no magnetic field). The temperature was kept fairly low, between 10^{-2} and 10^{-3} eV. Even at these low temperatures, the the deviation of the forces from the zero temperature value is on the order of .01% (if the energy or free energy were used by itself instead of averaging the two the deviation would be an order of magnitude worse).

The large number of k-points and diagonalization required to determine the eigenvalues makes the tight-binding Hamiltonian several orders of magnitude slower than the Stillinger-Weber potential.

2.3.3 Effective Hamiltonian for $PbTiO_3$

The potential function for $PbTiO_3$ is different in spirit from the silicon potentials. Lead titanate has five atoms in each unit cell, with three different species. To explicitly take into account the interactions between individual atoms, as was done for both potentials for silicon, would be very difficult to do well, and would ignore the physics that underlies the piezoelectric properties of the material. So instead the approach is to formulate an effective Hamiltonian for the unit cell that does not use empirical input and captures in a controlled and consistent manner the important properties such as the coupling between strain and electric field, and the ability for polarization switching to occur [39].

Understanding the energy functional for $PbTiO_3$ requires familiarity with the atomic structure of the material. At temperatures above 760 K, $PbTiO_3$ is in a paraelectric cubic perovskite structure, shown in Fig. 2.3. Atoms at the corners of the unit cell are lead, ones at the center of faces are oxygen, and the one at the center is titanium. Below 760 K, $PbTiO_3$ is piezoelectric, and has a non-centrosymmetric tetragonal crystal structure, with a spontaneous polarization along the (001) direction or along one of the five other symmetrically equivalent directions of the paraelectric phase. In addition to the lowest energy tetragonal phase, there are other minima in the energy of $PbTiO_3$ with respect to polarization direction. The orthorhombic phase has polarization in the (011) or equivalent direction, and the rhombohedral phase had polarization in the (111) or equivalent direction.

The effective Hamiltonian we use was developed by Waghmare and Rabe [39]. Essentially it is a Taylor expansion about the paraelectric phase that is a function of the strain $e_{\alpha\beta}$, the electric field $\vec{E}$, and internal degrees of freedom of the unit cell. Not all the internal degrees of freedom are tracked explicitly; only those that are associated with the unstable zero frequency phonons in the paraelectric phase are included in the effective Hamiltonian. These phonons are linear combinations of uniform atomic displacements that span a three-dimensional subspace that corresponds to the lowest energy internal distortions of the cubic structure. These atomic displacements are written as as the vector $\vec{\xi}$ in the effective Hamiltonian; a precise expression for $\vec{\xi}$ in terms of the atomic displacements are given in Ref. [39].

An explicit form of the energy expansion is obtained by demanding it to be

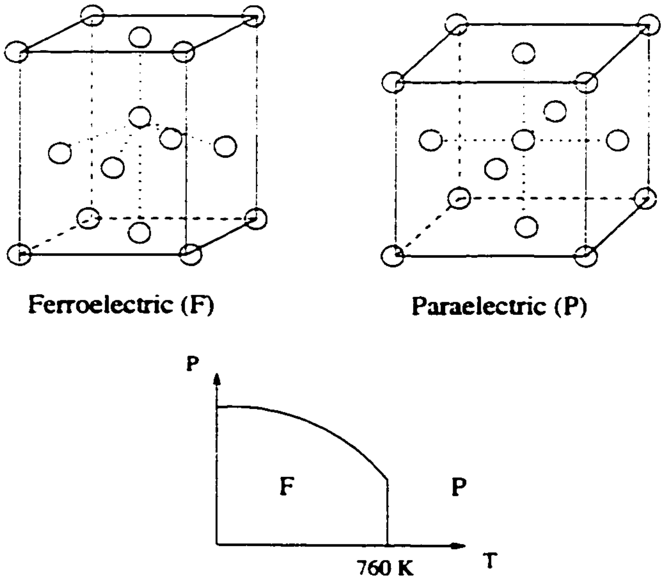

Figure 2.3: Perovskite crystal structure of $PbTiO_3$: Above $T = 760$ K, the structure has cubic symmetry corresponding to paraelectric phase and at low temperature, it becomes non-centrosymmetric tetragonal corresponding to the ferroelectric (piezoelectric) phase. The transition between the two phases is of first-order and is characterized by a nonzero order parameter, polarization P, in the ferroelectric phase.

invariant under cubic symmetry and making use of symmetry properties of $e_{\alpha\beta}$ and $\vec{\xi}$,

$$\begin{aligned} E_{tot} &= \frac{1}{2}C_{11}\sum_{\alpha} e_{\alpha\alpha}^2 + \frac{1}{2}C_{12}\sum_{\alpha\neq\beta} e_{\alpha\alpha}e_{\beta\beta} + \frac{1}{4}C_{44}\sum_{\alpha\neq\beta} e_{\alpha\beta}^2 + f\sum_{\alpha} e_{\alpha\alpha} \\ &+ g_0(\sum_{\alpha} e_{\alpha\alpha})|\vec{\xi}|^2 + g_1\sum_{\alpha}(e_{\alpha\alpha}\xi_{\alpha}^2) + g_2\sum_{\alpha<\beta} e_{\alpha\beta}\xi_{\alpha}\xi_{\beta} \\ &+ \tilde{A}|\vec{\xi}|^2 + B|\vec{\xi}|^4 + C(\xi_x^4 + \xi_y^4 + \xi_z^4) + D|\vec{\xi}|^6 + E|\vec{\xi}|^8 \\ &- Z\sum_{\alpha}\xi_{\alpha}E_{\alpha} - \frac{\Omega}{8\pi}\epsilon^{\infty}\sum_{\alpha}E_{\alpha}^2. \end{aligned} \tag{2.40}$$

The constants $C_{\alpha\beta}$ are elastic constants, g_i are the couplings between strain and atomic displacements. $\tilde{A}$ is the harmonic force constant for $\vec{\xi}$, B, C, D, E are anharmonic coefficients, Z is the mode effective charge, Ω is the unit cell volume and ϵ^{∞} is the dielectric constant. The constant f is added to correct the 2% error that DFT calculations make in the determination of the lattice constant. This model is the projection of the model in Ref. [39] onto the subspace of uniform atomic displacements $\vec{\xi}$ (in other words, the phonons corresponding to the displacements $\vec{\xi}$ are gamma point phonons). Also, appropriate terms added to allow for interaction with electric field. Polarization is given by

$$P_{\alpha} = Z\xi_{\alpha} + \frac{1}{4\pi}(\epsilon^{\infty} - 1)E_{\alpha}. \tag{2.41}$$

Due to the finite temperature ferroelectric phase transition in $PbTiO_3$ (also linked with strong anharmonicity), its dielectric and piezoelectric response is strongly temperature dependent. The present approach can readily be generalized at finite temperature (T) through a free energy expansion. Due to symmetry, the form of the expansion remains the same, with the parameters being temperature dependent. In the present work, we use the phenomenological arguments of Landau's mean field theory [44] to absorb the temperature dependence in the $\tilde{A}$ parameter alone,

$$\tilde{A}(T) = A'(T - T_0). \tag{2.42}$$

The computed values for the coefficients in Eqs. 2.40 and 2.42 are given in Ref. [39]. All the coefficients are determined via density functional theory calculations;

there is no empirical input (except, of course, in the determination of f in Eq. 2.40). This approach is not only more controlled and consistent than using an phenomenological constitutive relation, but also permits systematic testing through overdetermination of these parameters [39].

From the energy density in Eq. 2.40, we can find the derivatives the the QCBC method requires. Equation 2.17 must be satisfied, which, in the notation of Eq. 2.40 is written,

$$\left.\frac{\partial W}{\partial \boldsymbol{\xi}}\right|_{\mathbf{F}} = 0. \tag{2.43}$$

Also, noting that the relation between the strain and deformation gradient is

$$\epsilon_{IJ} = \frac{1}{2}(\mathbf{F}_{iJ}\mathbf{F}_{iK} - \delta_{IJ}), \tag{2.44}$$

the Piola-Kirchoff stress (Eq. 2.9) can be calculated via Eq. 2.40.

We have described in detail the main computational method we will use: the local quasicontinuum method extended to handle complex Bravais crystals. We have also examined in detail the three atomic potentials we have implemented. The rest of this thesis focuses on application of this method to indentation of silicon and $PbTiO_3$.

Chapter 3

Silicon Indentation I

Indented silicon is a rich, challenging system, with large inhomogeneous stress fields due to the indenter interacting with a complicated, multi-welled microscopic energy surface. In their experimental work Clarke *et al.* observed evidence for phase transformations underneath the indenter [8]. Since then, several experimental and computational studies have helped to illuminate some aspects of the behavior of the system, but many unanswered questions remain. Here we apply the local quasicontinuum method extended to handle complex Bravais crystals to silicon indentation. With this method, we are able to incorporate into the simulation what we believe is the essential physics of the system: the rapidly varying strain fields caused by the indenter, strong elastic coupling between neighboring regions of the material, and a local energy surface that broadly captures the complexity of the true local energy surface. We aim to obtain a broad, though qualitative portrait of the microscopic and macroscopic behavior of the system.

In this chapter, we begin by discussing the previous experimental and computational studies of silicon indentation. We then proceed to discuss our preliminary simulation results, where we have two principal goals. First, since the local quasicontinuum method extended to handle complex Bravais crystals is a new, unexplored computational tool, we need to examine and understand the properties of the simulations in their own right, independent of experiment. We use two- and three- dimensional finite element meshes and two different atomic potentials in an effort to identify which results of a simulation are robust, and which are influenced by biases in the underlying potential, coarseness of the mesh, or limitations of other approximations made in the local quasicontinuum method. Second, as we begin to understand what we can trust, we make observations with the help of simulation results about the physical nature of the system, with an emphasis on microscopic behavior difficult to obtain via experiment.

In the next chapter we will focus on direct comparison between our simulations and experimental results.

3.1 Previous Work

The indentation of silicon has attracted a great deal of experimental attention since Clarke *et al.* observed a reversible drop in resistance across the indented region, suggesting a reversible transformation to a metallic form of silicon underneath the indenter [8]. Further support for this hypothesis was obtained by Pharr *et al.* [2, 3], who found hysteretic load vs. displacement and load vs. electric resistance curves. Spherical indenter studies by Weppelmann, *et al.* [1, 9] and Williams, *et al.* [12] using spherical indenters observed discontinuities in the load vs. displacement curves that they attributed to sudden phase transformations. Using Berkovich indenters, Mann, *et al.* observed discontinuities in load vs. displacement and resistance vs. displacement curves above a critical load that were also attributed to sudden phase transformations [11]. Finally, Kailer, *et al.* [10] utilized Raman spectroscopy to detect transformed phases that remain after full unloading and detected a several phases of silicon in the indented region. Groups also reported that indentation can create an amorphous phase, and this appears to depend on loading rate and the size of the indentation [8, 10, 11].

The experiments strongly suggest that a reversible phase transformation to a metallic form of silicon does occur during indentation. But the experiments thus far must rely on macroscopic measurements such as load vs. displacement curves to intuit what is happening underneath the indenter. Probes such as Raman spectroscopy are available to identify more directly the types of phases present, but presently it is only possible to use them after the indenter is unloaded, not *in-situ* while indentation proceeds. A variety of questions are left unanswered: what phases form during indentation? What is the size and geometry of the transformed region? How do the phase transformations give rise to the hysteresis and discontinuity in the load vs. displacement curves? How can the resistance measurements be understood? How does cracking affect the macroscopic measurements? Some of these open questions have motivated computational work on the system. However, the large size of the sample, coupled with the very large strains in the immediate vicinity of the indenter makes the problem extremely challenging from a computational point of view.

Studies of silicon nanoindentation by Kallman, *et al.* [22], were based on molecular dynamics simulations using the Stillinger-Weber interatomic potential [37]. They reported evidence for amorphization beneath the indenter, but detected no phase transformations to a metallic crystalline form. Due to the computational intensity of the simulation, these studies were restricted to a very small simulation cell with sides $\sim$ 20 nm. In addition, the loading rate was on the order of 10^3 m/s, between six and ten orders of magnitude faster than the experiments mentioned above. No simulated load vs. displacement or load vs. resistance curves were reported, making it difficult to compare with experiment and establish the validity of the simulation.

Perèz *et al.* [23] performed zero-temperature, quasistatic density functional theory (DFT) simulations of silicon nanoindentation. They observed the formation of interstitial defects and extrusion. The computationally intensive nature of these simulations restricted the cell to $\sim$ 2 nm on a side, and necessitated the use of an atomically sharp rigid indenter. They did not attempt to directly compare their results with experimental results.

At the other extreme, continuum finite element simulations using phenomenological constitutive models have been routinely used to study indentation. Bhattacharya and Nix [24], in one of the earliest works, studied nanoindentation into silicon, nickel and aluminum using a 2D axisymmetric model. The constitutive model used was that of an isotropic elastic-plastic material with linear strain hardening. More recent approaches, such as that of Knapp *et al.* [25] are fundamentally similar. The main limitation of these approaches, with regards to the current study, is that use of the simple phenomenological models leaves out the possibility of structural phase transformations.

Weppelmann *et al.* [1, 9] used an analytic continuum analysis of an elastic-plastic system where the plastic behavior was taken to result from phase transformations. There were several parameters that had to be determined from experiment to calculate quatities such as the mean pressure at the onset of the phase transformations. Their approach was not meant to be able to simulate the behavior of the system, but create a model to aid in the analysis of experimental results.

The sum of these computational and theoretical endeavors has not produced a load vs. resistance curve, while the simulated load vs. displacement curves do not capture important features of experimental curves, such as hysteretic loops or smooth curves interrupted by discontinuities.

3.2 Simulation Details

Expanding on the discussion on our computational method in the previous chapter, here we discuss the finite element mesh and some implementation details. We use a finite element mesh with constant-strain finite elements; the finite elements are triangles in the two-dimensional mesh, and tetrahedra in the three-dimensional simulations. The mesh is finest near the indenter, and coarser further away. No adaptation occurs in the course of a simulation. The boundary conditions of the finite element mesh are fixed on the bottom of the mesh, periodic on the sides, and free on the top surface (except where the indenter touches the mesh). All simulations are quasistatic: the center of the indenter is incrementally lowered toward the surface of the sample. and at each indenter depth the optimal positions of the nodes are determined by minimizing the energy of the system with a conjugate gradient algorithm.

The method described in Chap. 2 is general enough to handle unit cells of any size, but for convenience and computational efficiency we use a two atom unit cell for silicon. Then. for a given deformation gradient field the energy of each finite element must be minimized with respect to the relative position of these two atoms. according to Eq. 2.17. In the course of a simulations some the finite elements go unstable. and the relative positions of the basis atoms change by a large amount. which usually indicates that a phase transformation has occurred. To verify this, and to unambiguously identify the new phase, the deformation gradient and relative basis atom position of the candidate finite element is used to create an infinite silicon crystal. Off line, this crystal is allowed to relax, free from the constraints of the finite element mesh. It relaxes to the nearest local energy minima in configuration space, and the phase of the finite element is identified with the phase of this local minima. [1]

3.3 Two-dimensional Simulations

With a two-dimensional finite element mesh we are able to directly compare simulations using two different potentials. For each of the two potentials, the simulation setup–the finite element mesh, loading rate, parameters for the conjugate gradient algorithm, etc.–are exactly the same. We have implemented the Stillinger-Weber (SW) empirical potential [37], and the nonorthogonal tight-binding Hamiltonian of Bernstein and Kaxiras[38]. These two-dimensional simulations are not necessarily experimentally relevant. Our principal intent here is to focus on the properties and robustness of simulation results, apart from what the say about the physical world.

---

[1] This method of determining phases assumes that metastable states of silicon that form during indentation do not become unstable when allowed to relax at zero pressure. For silicon this assumption appears justified, but it is definitely not justified for $PbTiO_3$ (see Chap. 5).

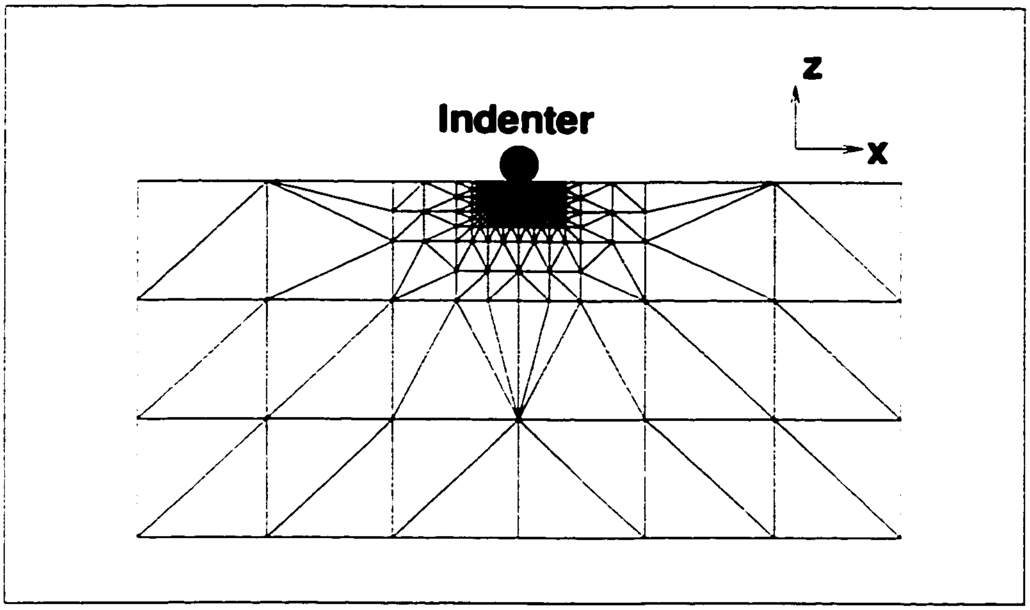

Figure 3.1: The finite element mesh used in two-dimensional simulations with the Stillinger-Weber potential and a tight-binding Hamiltonian.

Since the tight-binding Hamiltonian is so computationally intensive (see the discussion in Sec. 2.3.2) we are restricted to modest simulations. The mesh is shown in Fig. 3.1. We use a two-dimensional mesh with 556 elements; the indenter is circular with perfect stick boundary conditions. Close to the indenter the finite element size is about 1/5 the indenter radius, and the total size of the mesh is about 20 times the indenter radius. Nodes not constrained by boundary conditions or stuck to the indenter are free to move in the xz plane. Simulations were run where these nodes were also permitted to move in the y-direction, and others where they were not. No substantial difference was observed. In the results shown, displacement in the direction perpendicular to the plane of the mesh was permitted.

The crystallographic $[\bar{3}12]$ direction of silicon was oriented along the x-axis in Fig. 3.1, and the $[111]$ direction was directed along the z-axis. We explored other crystallographic orientations, but find that our conclusions do not depend on the crystallographic orientation.

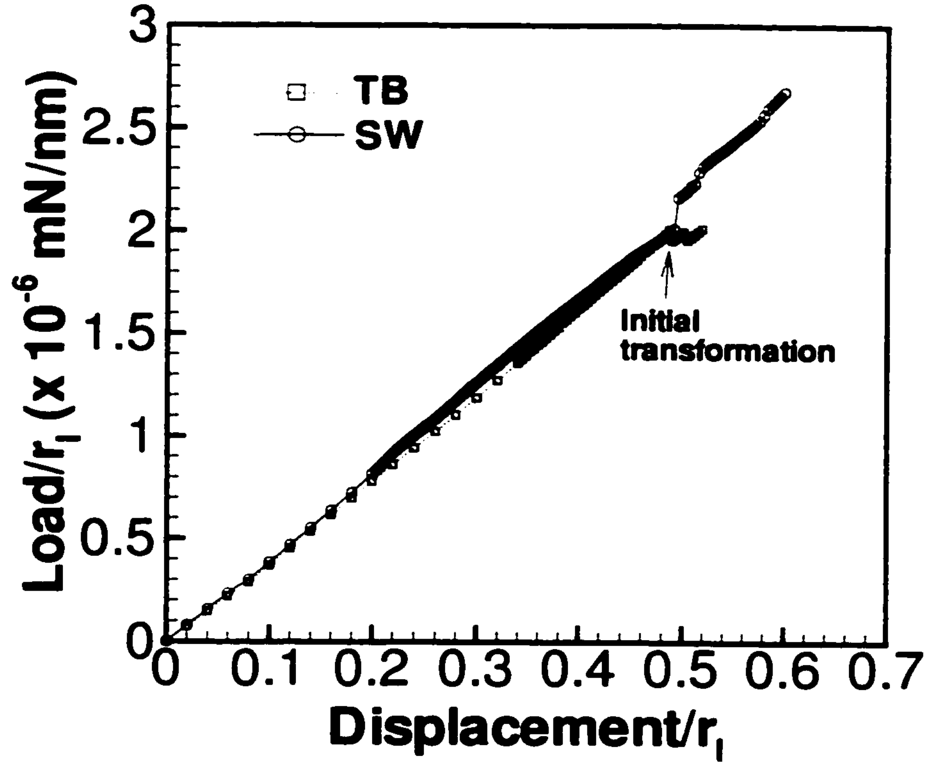

Figure 3.2: Comparison of the load vs. displacement curves obtained from simulations using the Stillinger-Weber potential and a tight-binding Hamiltonian.

Before phase transformations occur, both potentials give similar load vs. displacement curves, as shown in Fig. 3.2. In the two-dimensional simulations, the onset of phase transformations are marked by discontinuities in the curves. The phase transformations begin at the same indentation depth and load. Snapshots of the mesh after high pressure phases have begun forming are shown in Fig. 3.3. Figs. 3.3 (a) and (b) show the shear strain, ϵ_{xz} for the two potentials. Qualitatively the two are similar, both showing two concentrations of shear strain symmetric about the z axis beneath the surface. For both potentials, these concentrations occur at the edges of the phase transformed region; Figs. 3.3 (c) and (d) show the finite elements that have transformed. The different colors of the finite elements correspond to different phases. Light blue is diamond silicon; yellow is bct5; white is body-centered cubic, and red is a form of bct5 with a stacking fault.

An obvious difference between the two simulations is that the phases are different. It is not surprising that the types of phases that form depend on the potential chosen. The energy surface of this system as a whole is extremely complicated, and any subtle biases or flaws in the interatomic potential can affect which energy well an element moves into under the influence of the surrounding medium. In particular, it is well known that the SW potential too enthusiastically favors the Bct5 structure, which is reflected in our results here [45]. The flaws revealed in the TB Hamiltonian are also severe. The Bct5 structure with a stacking fault should not even be stable, according to density functional theory calculations.

Nevertheless, there remain several similarities between the two simulations. For example, the transformed regions have the same qualitative shape. The anisotropy of the crystal affects the transformed region in the same way, favoring transformations in the negative x half-space. Also, in both there tends to be a clustering of like phases.

That simulations using these two very different interatomic potentials produce a transformed region whose shape and clustering properties are similar hint that these features are robust results of the simulations. Further studies using three-dimensional meshes

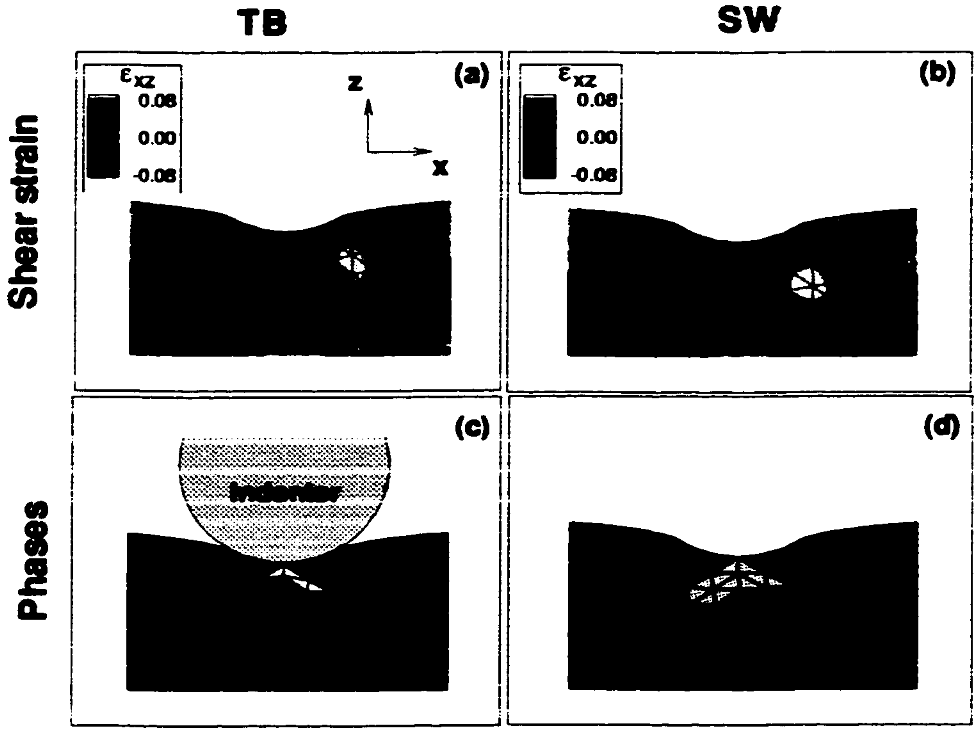

Figure 3.3: Comparison of snapshots of the finite element mesh soon after phase transformations have begun. Results using the Stillinger-Weber potential and a tight-binding Hamiltonian are shown. The figures show the shear strain ϵ_{xz} ((a) and (b)), and the phases that have formed ((c) and (d)). The phases that correspond to each color in (c) and (d) are discussed in the text.

confirm this. The macroscopic measures, including the onset of phase transformations, also appear to be robust. However, it is clear that we cannot expect to determine the phases that appear underneath the indenter, as this clearly depends on the potential.

As a final point, it is interesting to note that the tight-binding Hamiltonian is not obviously more accurate than the SW potential. The SW potential makes no attempt to model the electrons explicitly, but instead relies on a physical understanding of the bonding properties of solid silicon, and this motivates a simple functional form. The tight-binding Hamiltonian does model the electrons explicitly, and one would expect this to make the Hamiltonian more accurate, or at least more transferable. But for the purposes of the QCBC method, neither potential has a clear advantage. This might in part be because the QCBC method is very demanding of the atomic potential it utilizes. The tight-binding Hamiltonian does give superior results when compared to the SW potential for a number of important properties of silicon, particularly for those related to defects and interfaces [38]. However, in the course of a simulation the QCBC method samples a wide swath of the configuration space of a two-atom unit cell, and apparently this type of sampling neither potential is obviously superior. This, coupled with the fact that the SW potential is significantly faster than the TB Hamiltonian, motivates us to use the SW potential exclusively for the rest of our study.

3.4 Simulations with a Three Dimensional Mesh

In this section we explore some preliminary results of simulations using a far more realistic and computationally intensive three-dimensional finite element mesh. We discuss typical load vs. displacement curves, and the evolution of the phase transformed region in the course of loading and unloading. Where justified we make observations about the simulations that may indicate behavior of the physical system, in an attempt to provide information currently difficult to obtain via experiment.

An important aspect of this section is the continued skeptical examination of our method. In particular. we focus on how mesh spacing and orientation affect simulation results. We do not use the tight-binding Hamiltonian since it is not obviously superior to the SW potential (as discussed in the previous section), and is several orders of magnitude slower. Simulation times would be prohibitive since the the three-dimensional mesh has two orders of magnitude more finite elements than the two-dimensional mesh.

Direct comparison with experimental results. and in particular a discussion of load vs. resistance curves. will be the focus of the next section.

Before proceeding to our results we briefly mention some methodological details beyond those already discussed in Sec. 3.2. The indenter is modelled as a spherical force field [46]. so the the total energy is a sum of the strain energy of the finite element mesh, U_M, and the energy due to the indenter. U_I:

$$U_{Tot} = U_M + U_I = U_M + \frac{\alpha}{2}\sum_j \left(\frac{r_I - |\vec{r}_I - \vec{r}_j|}{r_I}\right)^n \theta(r_I - |\vec{r}_I - \vec{r}_j|) \qquad (3.1)$$

where θ is the Heavyside step function, r_I is the indenter radius. and $\vec{r}_I$ and $\vec{r}_j$ are the position vectors of the center of the indenter and the node j of the finite element mesh, respectively. This spherical force field has some useful qualities. First. it is easy to implement and numerically stable. Other simple schemes such as rigid perfect stick indenters, where the indenter is infinitely hard and nodes are not allowed to move across the surface of the indenter when touching it, can give some spurious results, particularly over repeated loading and unloading cycles. Second, the spherical force field imposes no tangential force on the nodes: in this sense it is a model for a frictionless indenter. This means that under certain conditions the linear elastic simulation results can be compared with the theoretical results of Hertz [47], who determined the linear elastic response of a system indented with a frictionless indenter.

Unfortunately, for no choice of the coefficient α and the exponent n is an elastic indenter perfectly modelled. The indenter in Eq. 3.1 is like a sphere of independent springs, each with one end attached to the center of the indenter, and the other end attached to a node located less than a distance r_I away from the center of the indenter.

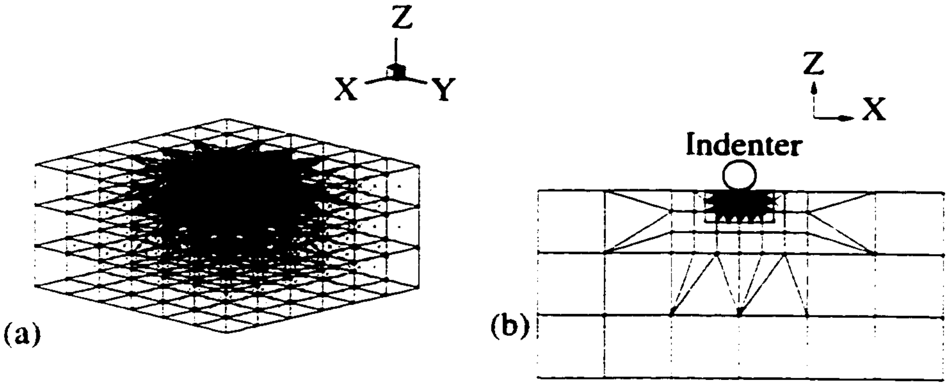

Figure 3.4: The three-dimensional medium fine finite element mesh (a) and a slice through it at $x = 0$ (b).

The springs are free to rotate around the center of the indenter at constant length, but resist with a $n - 1$ force law when moved in the normal direction. There is no coupling between the springs, and this is unphysical. If the indenter were modelled accurately, a compressed spring, for example, should make it easier for a neighboring spring to compress. To accurately model the indenter would require a full finite element treatment. However, since treating the indenter as in Eq. 3.1 is numerically efficient and stable, and since we do not seek quantitative accuracy, modelling the indenter with a finite element mesh would be misplaced effort.

With silicon, our strategy is to make the indenter as hard as possible without adversely affecting the numerical performance of the conjugate gradients solver. The exponent n was chosen to be 4, and α was chosen to be 4×10^9 eV. Even in the deepest simulated indentations the maximum amount nodes moved into the indenter was about 2% of the indenter radius. It is possible to more closely mimic the behavior of an elastic indenter, and we will do that for piezoelectric indentation in Chap. 5. The principal reason we do not do it for silicon is that there is not sufficient published information about the experimental setup to enable us to model the indenter used in experiment. Also, by making the indenter very hard, our simulations ought to reproduce the Hertzian load vs. displacement curve, a useful check on our simulation.

If we make the finite element mesh finer, or rotate it with respect to the underlying crystal, the physics of the system does not change, so we would expect the simulation results to remain the same. However, the constraints and modification of the rotational and translational symmetry of the system introduced by the mesh does affect the simulation, and it is crucial that we determine the extent of this effect. To this end, we performed a number of simulations to explore which behaviors observed in the simulation are robust, and which depend on details of the mesh. Three mesh spacings are used and their results compared: in the least fine, the dimensions of the smallest finite element are 1/5 the indenter radius; in the medium fine mesh the smallest finite element size is 1/9 the indenter radius (this finite element mesh is shown in Fig. 3.4); in the very fine mesh the smallest finite element size is 1/13 the indenter radius. For these simulations, the [111] crystallographic direction of silicon points along the z-axis. In most of the simulations, the $[\bar{2}11]$ direction points along the x-axis, but in one simulation, to test for how orientation of the mesh affects results, the $[\bar{5}41]$ direction points along the x-axis (this mesh as subsequently referred to as the rotated mesh).

3.4.1 Comparing Results from Different Meshes

In Fig. 3.5 shows a load vs. displacement curve from a simulations that uses the least fine mesh. Since there is no absolute length scale in the simulations, the simulation results are scaled to the indenter radius r_I. Fig. 3.5 shows a deep indentation, with the maximum depth about 1/2 the indenter radius. The most striking feature of the load vs. displacement curve is the reproducible hysteresis loop, a feature that has been observed in some experiments [2, 3]. The hysteretic behavior in the simulation curve in Fig. 3.5 is due to the formation and disappearance of metallic silicon phases beneath the indenter. This is the same mechanism presumed to cause the hysteresis in load vs. displacement curves in experiment [2].

Even using this relatively coarse mesh, our simulations exhibit reversible phase

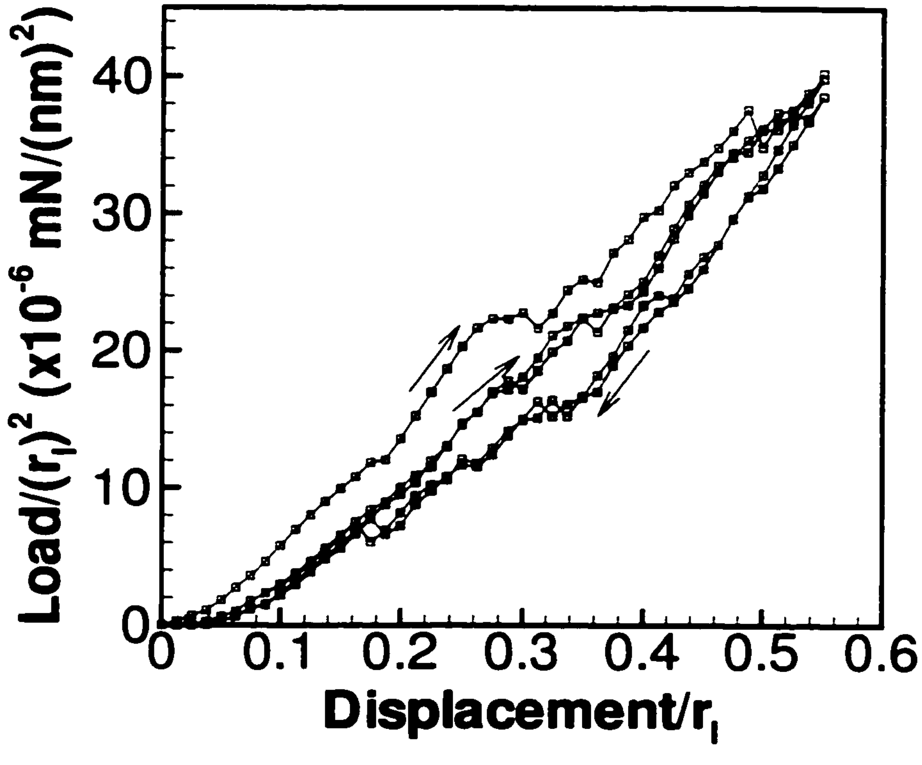

Figure 3.5: The load vs. displacement curve obtained using the least fine mesh. The data is scaled by the indenter radius, r_I.

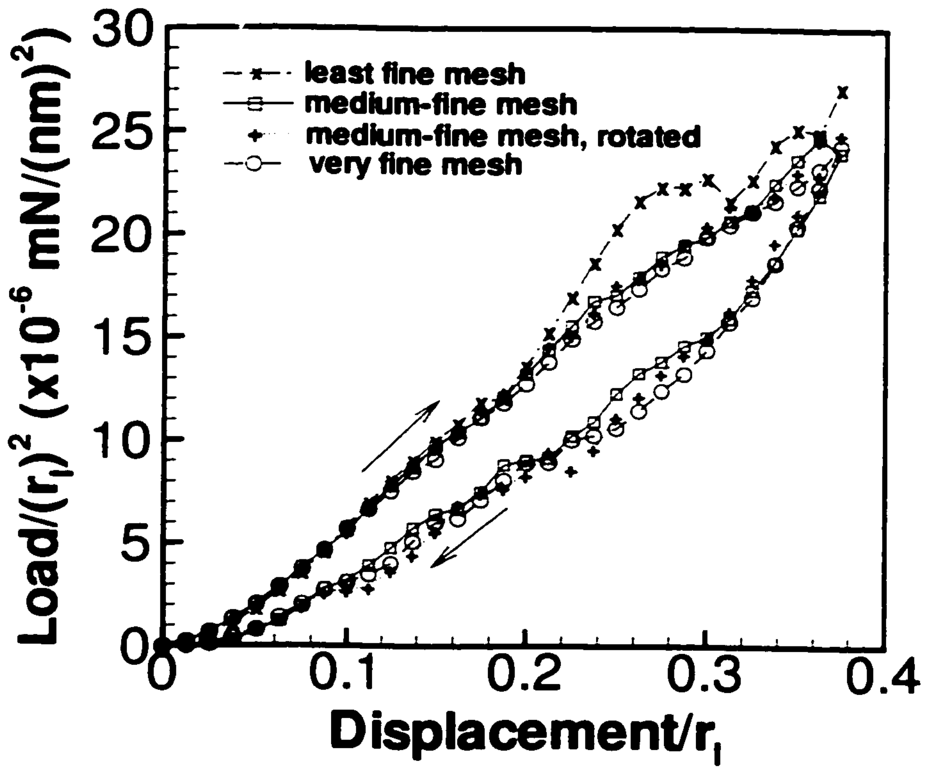

Figure 3.6: A comparison of load vs. displacement curves for several different meshes.

transformations underneath the indenter and a reproducible hysteresis loop. Previous computational models have not been able to produce these features. However, some qualitative features of the simulation curve are very different from experiment. For example, the simulation curve is very jagged, while experimental curves tend to be mostly smooth. One possible explanation has to do with the finite size of the finite elements. The size of the finite element sets the minimum volume over which a transformation can occur, and the larger the volume, the larger the perturbation of the system when the transformation occurs. This leads us to compare load vs. displacement curves for a range of mesh spacings.

Fig. 3.6 shows a comparison of the load vs. displacement curve for simulations using the least fine mesh, a medium fine mesh, a rotated medium fine mesh, and a very fine mesh. Details about these finite element meshes are discussed in the previous section. The curve from the coarsest mesh is significantly different from the others. suggesting that the coarse mesh is not converged with respect to mesh spacing. All subsequent discussion will not include results from simulations using the least fine mesh. The other load vs. displacement curves are significantly smoother, and all exhibit the same basic features and magnitude. For a sufficiently fine mesh the macroscopic load vs. displacement curve is fairly robust. unaffected by perturbations introduced by modifying the mesh or potential.

Without exception. in all the simulations several phases form beneath the indenter. These silicon phases include a five-fold coordinated form of metallic silicon (bct5) [45], β−Sn, simple cubic, and body-centered cubic. In addition. several non-physical phases appear that are stable for SW silicon, but are not stable according to density functional theory. In the nanoindentation simulations, the only non-physical phase that appears in any appreciable amount is a layered hexagonal structure. Generally, bct5, followed by β−Sn and a non-physical hexagonal structure are the most prevalent phases that form upon loading, while bct5 and simple cubic are the most prevalent upon unloading. All of the non-diamond phases are metallic, according to density functional theory calculations.

Physically, it is reasonable that many phases, not just a single transformed phase, would form under the indenter. The energy surface of the two-atom silicon unit cell is very complicated, with a large number of local minima corresponding to different phases. The indenter imposes large, rapidly varying strain fields in its vicinity that, in conjunction with the strong elastic coupling between finite elements spread the finite elements in the system over an extended region of configurational phase space of the silicon unit cell. This broad sampling of configurational phase space places the finite elements into a variety of different local minima. It is possible, however, that the formation of cracks or defects would modify this behavior.

At this juncture we are particularly interested in the details of the phase distribution. From our discussion of the two-dimensional simulations, we do not expect our three-dimensional simulations using the SW potential to produce the same phases that simulations using a different potential would produce. This sensitivity on the potential indicates also that we should not expect them to reproduce the phases found in experiments. But to what degree are the phases found in the the simulation independent of the details of the mesh? And what might we be able to learn from this line of inquiry about the physical nature of the system?

We use two simple tools. First, we examine the evolution of the number of finite elements of various phases as a function of indentation depth. Second, we track the size and number of clusters during an indentation cycle. A "cluster" is a group of contiguous finite elements of the same phase, each of which is connected to another element of the group by at least one finite element face. With these tools we hope to explore the geometry of the transformed region, something the simulations using a two-dimensional mesh suggest may be a robust feature of our simulations.

Fig. 3.7 compares the number of finite elements of the bct5, $\beta-$Sn, and simple cubic phase of silicon in the course of a simulation for the medium fine, rotated medium fine, and very fine mesh. The data from the finest mesh is scaled by the ratio of the finite element volumes to facilitate direct comparison. The indenter is loaded until reaching a depth of 3/8 of the indenter radius, then the system is unloaded.

The basic shape and scale of the curves, the load at the initial transformation, and the final unloaded values are more or less independent of the mesh spacing and orientation. Also consistent are basic features such as the minimum in the simple cubic phase curve during the unloading phase, the saturation of the number of bct5 elements upon unloading, and the steep increase in the number of β-Sn elements upon loading. The phases that are present upon complete unloading are responsible for the hysteresis and residual deformation evident in the load vs. displacement curves. There are quantitative differences between the various simulations, particularly for the simple cubic phase, where there are fewer participating finite elements.

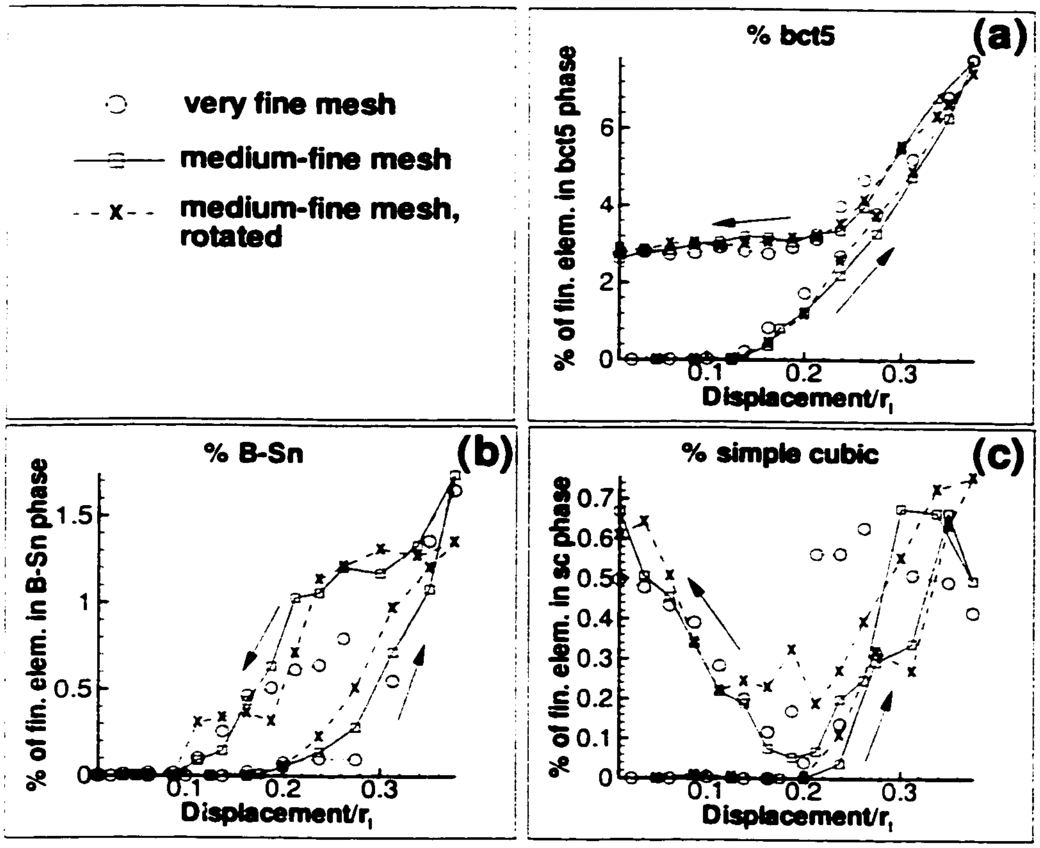

Figure 3.7: A comparison of the development of the numbers of finite elements of different phases. Three different meshes are used: a medium fine mesh, a rotated medium fine mesh, and a very fine mesh.

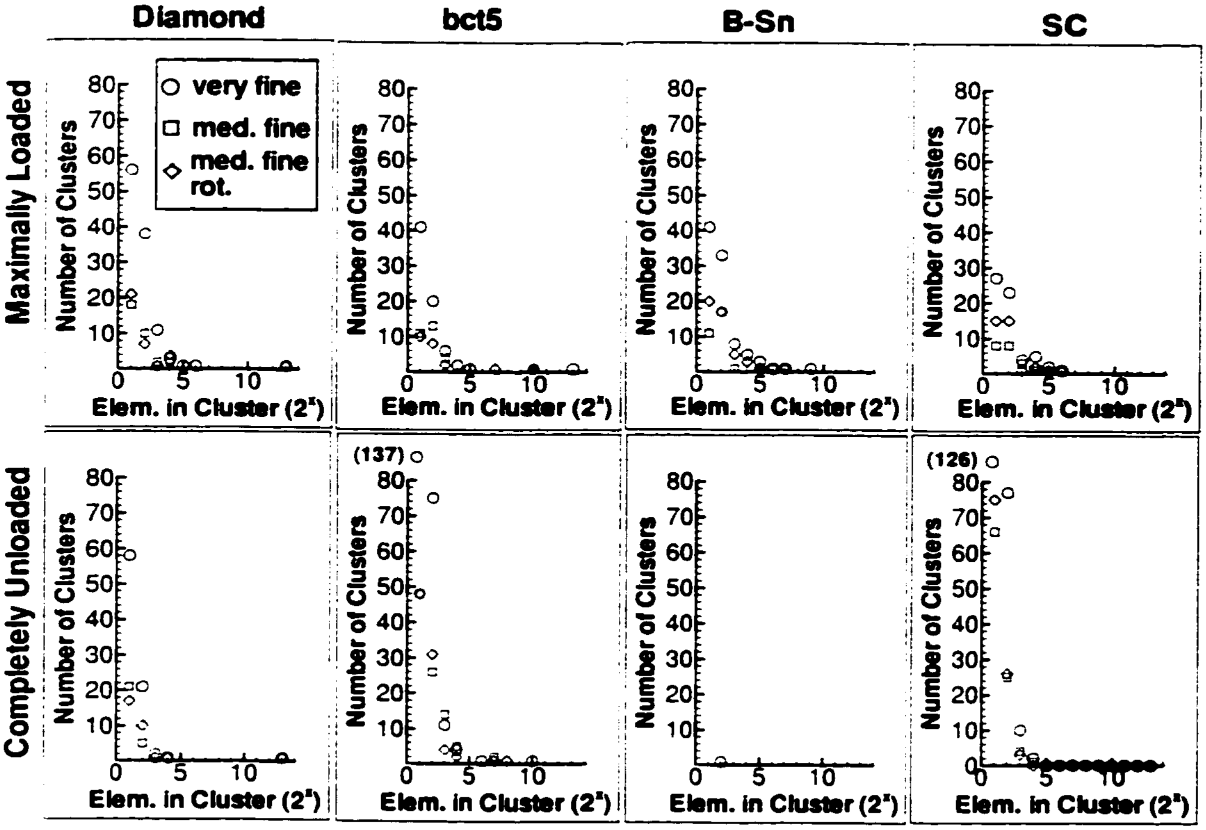

Figure 3.8: A comparison of the cluster distribution for several phases of silicon among simulations using a fine mesh, a fine rotated mesh, and very fine mesh. The plots are logarithmic histograms; integer position x on the horizontal axis indicates that the cluster has size n such that $2^{(x-1)} \leq n < 2^x$. Symbols are plotted only if there is at least one cluster corresponding to the integer x.

We also compare the cluster distribution of the three different systems. We find that rotating the mesh has no significant effect. but that mesh fineness does affect aspects of the evolution. In Fig. 3.8, the cluster distribution of diamond silicon, bct5, β-Sn, and simple cubic silicon are shown for the three meshes when the system is maximally loaded, and for when it is subsequently completely unloaded. The cluster sizes are expressed as the number of finite elements in each cluster. Here, the cluster sizes from the simulations using the very fine mesh are not scaled by the ratio of the finite element volumes. The profile from simulations using the two medium fine meshes are similar in all cases.

However. the profile from the very fine mesh simulation is different from the other two in one important respect. Since the cluster size is not scaled, it is to be expected that the large cluster of bct5, for example, in the very fine mesh is larger than the large clusters in the other two simulations. The significant difference becomes apparent when comparing the number of small clusters. If the system were converged at the medium fine mesh, then upon making the mesh finer, these very small clusters (consisting of one or two elements), would tend to become clusters with a larger number of elements in them. From Fig. 3.8, clearly that is not what is happening; the finer mesh has significantly more very small clusters.

We can make two observations about the results of the evolution of the number of finite elements of each phase (Fig. 3.7) and their clustering properties (Fig. 3.8). First, though there are quantitative differences in these microscopic results, these differences do not significantly affect the macroscopic results. Referring back to Fig. 3.6, the macroscopic measures are very similar (except, of course, for the unconverged coarse mesh simulation results). In particular, the loads and at the maximum indentation depth are very close, even though the exact number of phases, and the details of the clustering distribution are different. This implies that the energy surface of the system as a whole is degenerate: at a given indentation depth, there are a number of ways to arrange the various phases underneath the indenter to give similar macroscopic measures. The perturbations introduced by modifying mesh direct the system toward a different region of the degenerate phase space. This degeneracy is not surprising. It is likely due to the complicated nature of the the microscopic energy surface, and the strong elastic coupling between regions in the sample.

Second, the comparison of the small cluster profiles among simulations using the medium fine and very fine meshes indicates regions of fragmentation that may be sites of interesting physics. This fragmentation suggests that the system is frustrated. Based on the complicated interaction between the large strain field due to the indenter, the complicated microscopic energy surface, and the strong elastic coupling between regions, it seems reasonable that there would be some volumes made up of multiple finite element that would be able to settle down into a single energy minima of the silicon two-atom unit cell, and other frustrated regions where the competing constraints prevent neighboring finite elements from moving to the same microscopic state. That is exactly what is observed in the simulations, particularly in the fully loaded state.

Unfortunately it is these fragmented areas where the limitations of the simulation method are most apparent. Where different phases are in contact with each other, approximations such as neglect of interface energy, and constraining the structure to a two-atom basis become problematic. But even with these approximations in place, there is still an interesting question to explore in the future: if the mesh becomes increasingly fine, do multiple element clusters begin to form, or more and more one element clusters?

It is both tantalizing and frustrating to speculate on how these behaviors in the simulation may connect with experimental systems. The physical properties discussed above–the large strain fields, the complicated microscopic energy surface, and the strong elastic coupling–that likely cause the degeneracy and fragmentation in the simulation are also going to be properties of the physical system. But in the physical system, there are important processes left out of the simulation. How does the degeneracy of system affect and how it is affected by the generation of cracks and defects? How big are the energy barriers separating local minima in the degenerate landscape, or in other words,

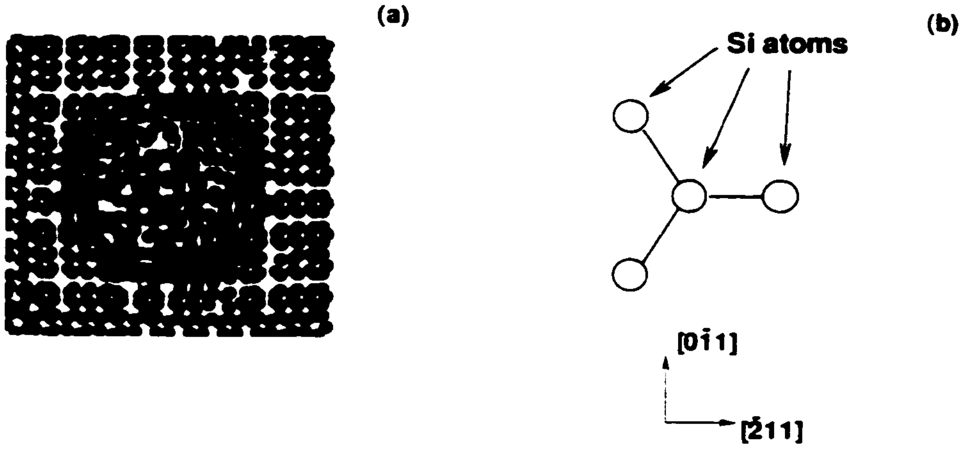

Figure 3.9: A slice through the finite element mesh during indentation (a), and the underlying crystalline structure in the simulation (b). In (a), each dot corresponds to a finite element. Dark finite elements are in in the diamond phase, lighter shaded finite elements have undergone phase transformations.

how would finite temperature affect the system's behavior? If fragmentation were to occur even if the finite element size became infinitely small, what would that correspond to in the experiments? The amorphization observed by some groups [8, 10, 11]? Defect sources? Nothing at all interesting? These questions all require further investigation.

We can now summerize our exploration of the robustness of our method. We used simulations simulations with two- and three-dimensional meshes, and explored the influence of the underlying potential and mesh parameters. We find that macroscopic measures appear to be robust. The initial onset of transformation to metallic phases, and the evolution of the size and clustering properties of the transformed region also appear to be consistent. The specific phases that form, however, depend on the potential.

3.4.2 Focus on a Single Simulation

We now make a more thorough examination of results from a simulation that uses the medium fine mesh. Keeping in mind the limitations of the simulations, we will explore some of the microscopic features of this simulation.

The distribution of phases under the indenter is influenced by the underlying crystalline anisotropy. Fig. 3.9 shows a cross section of the finite element mesh. a cut in the xy-plane near the indenter. Each dot corresponds to a finite element. The light grey circles correspond to finite elements that remain in the diamond phase. and the dark circles correspond to finite elements that have transformed to a metallic phase. Also in Fig. 3.9, the orientation of the crystalline lattice is shown. Clearly, the three-fold symmetry of the transformed region corresponds to the positions of the three tetrahedral atoms. This is not a mesh effect. If the mesh is made finer, or if it is rotated about the [111] direction, the effect persists.

We can again look at the evolution of the amount of phases and clustering as we did earlier in Figs. 3.7 and 3.8. Here, we will focus on a simulation with two loading cycles. Fig. 3.10 shows the how the number of finite elements of diamond, bct5, β−Sn, and simple cubic phases changes during the loading/unloading process. The development of the various phases over the first loading/unloading cycle is similar to that observed in Fig. 3.7. During the second loading the curve initially follows the unloading curve, but at some point switches over and begins to follow more closely the initial loading curve. But it does not follow the initial loading curve exactly, and in particular, comparing the first and second loading cycle at the maximum indentation depth there is a clear difference in the number of finite elements of some of the phases. The macroscopic load, however, is almost exactly the same, another indication that the energy surface is degenerate.

Studying the clustering of phases reveals a change in morphology of the clusters during a load/unload cycle. Fig. 3.11 shows the number and size of bct5 clusters at different points in the simulation. Upon initial loading, a single large cluster forms, with only a few small clusters present. At maximum displacement, nearly all ($>$ 90%) of the mass is in the single large cluster. However, upon unloading, the single large cluster begins to shrink and breaks in two, while the number of small clusters continues to increase. When fully unloaded, the bct5 cluster distribution is more fragmented, with 1/3 of the

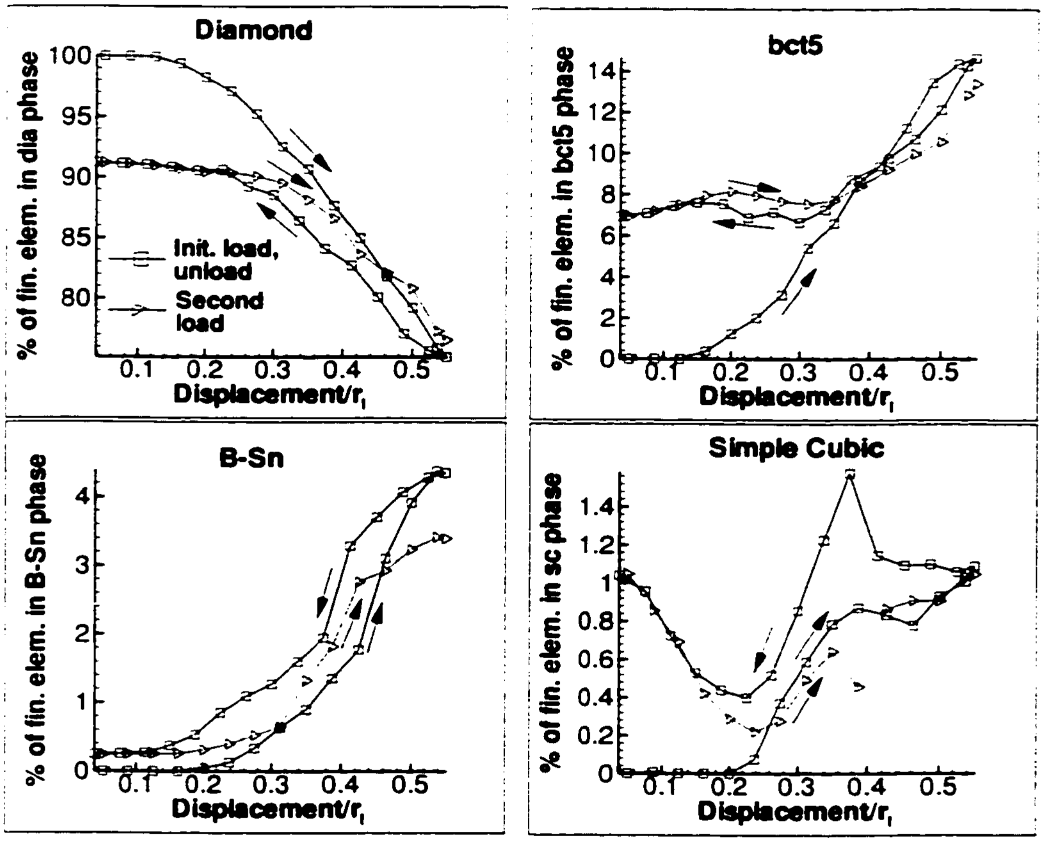

Figure 3.10: The development of the number of finite elements of the most common phases over repeated loads.

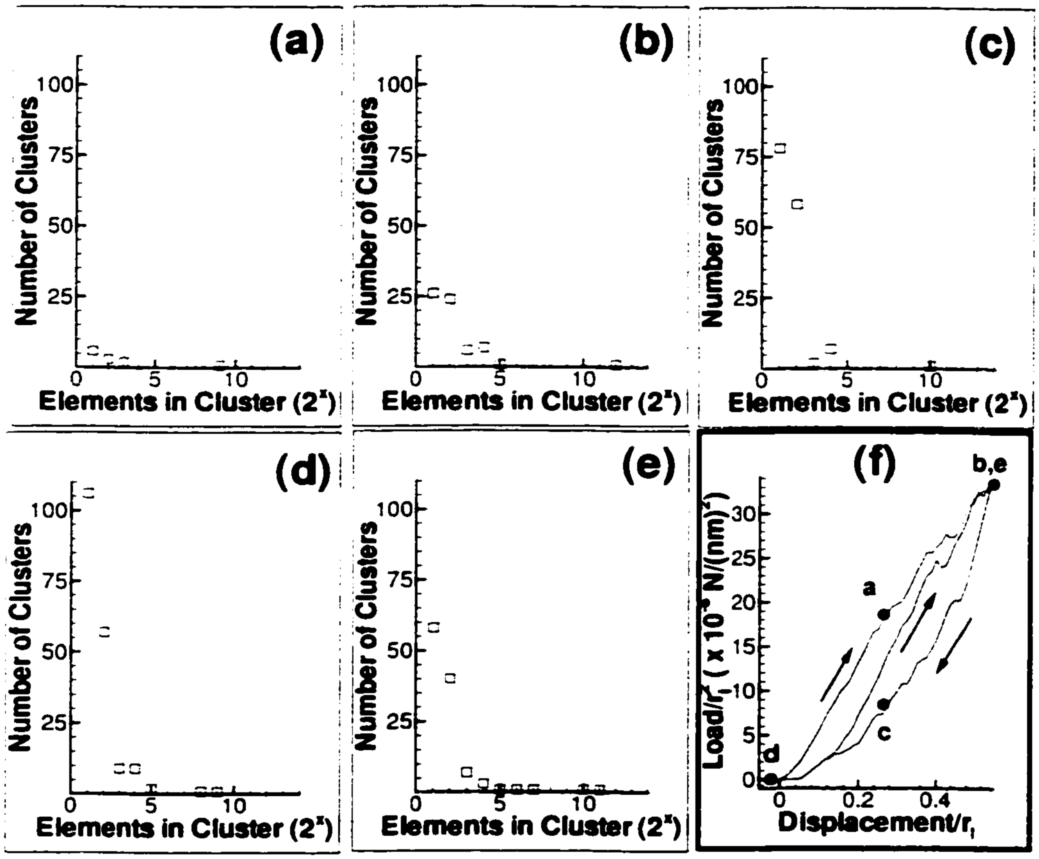

Figure 3.11: Evolution of bct5 clusters during a simulation. The panels (a) through (e) correspond to indenter positions labelled in panel (f). Plots (a) through (e) are binned as in Fig. 3.8.

mass in small clusters. When loaded again, the cluster distribution remains significantly more fragmented compared to the initial loading.

This general pattern of growing clusters upon loading and fragmentation upon unloading is common to all the phases. In addition to these changes in the distribution of clusters, the geometry of the largest clusters also changes dramatically during a load/unload cycle. If we consider all the transformed finite elements taken together, when fully loaded a well-connected, roughly hemispherical cluster forms underneath the indenter; when full fully unloaded, the largest connected cluster is stringy and tenuously connected. The difference is evident in Fig. 3.12. This figure compares two slices in the xy plane, one

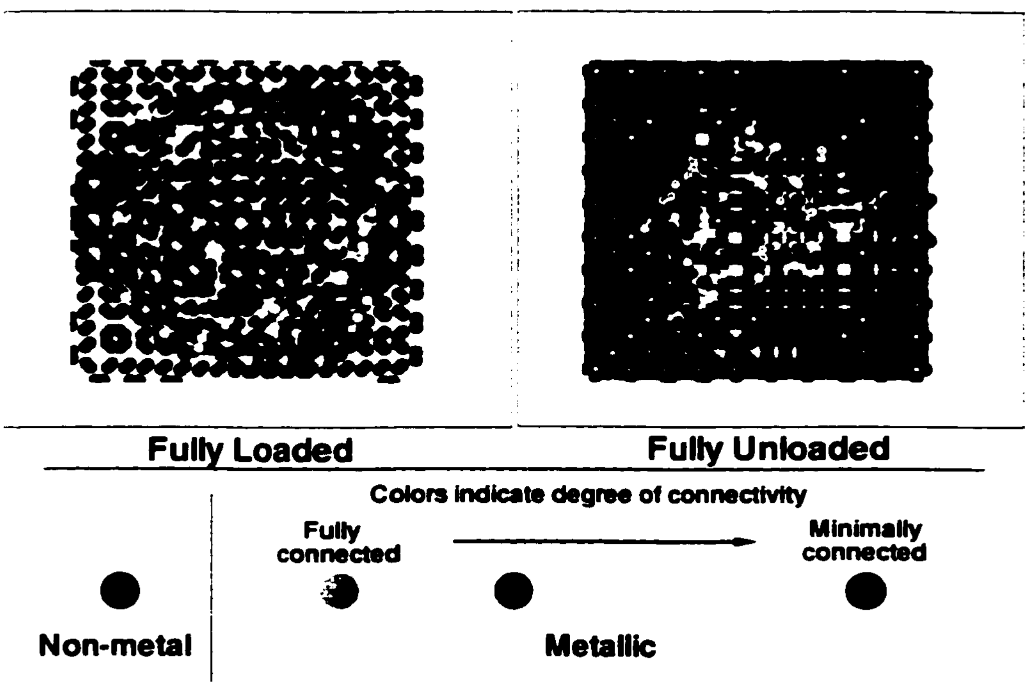

Figure 3.12: A comparison of the geometry of the largest metallic cluster in a fully loaded and completely unloaded system. Two slices through the 3-D mesh, like the one in Fig. 3.9, are snown.

of which is from a fully loaded sample, the other from a fully unloaded sample. Again, a dot corresponds to a finite element. Finite elements that are not part of the largest connected transformed cluster are colored blue. The other finite elements are constituents in the largest transformed cluster and are colored according to the number of finite element faces they share with other transformed elements in that cluster: those that are fully connected to other transformed finite elements are colored light blue, those that share three faces are colored green, those that share two faces are colored yellow, and those that are connected to the cluster by only one face are colored red. It is clear that the cluster at full unloading is much stringier and more tenuously connected than that of the fully loaded system. We keep this behavior of the largest conducting cluster in mind when we model resistance measurements in the next chapter.

3.5 Discussion

In this Chapter we began with several tests of the local quasicontinuum method applied to indentation of silicon. Using two different interatomic potentials and several finite element meshes, we conclude that we can trust the macroscopic curves and geometry of the metallic cluster that forms underneath the indenter, but not the specific types of phases that form.

With these limitations in mind, we were able to make several observations about the microscopic behavior of the system, such as the observation that many phases form underneath the indenter for deep indentations; that the three-fold symmetry of the silicon unit cell about the (111) direction influences the geometry of the phase transformed region; and that the roughly hemispherical transformed region that forms upon loading fragments upon unloading. We also observed that the energy surface of the system appears to be degenerate. How physical processes left out of the quasicontinuum method, such as defect or crack formation, affect these observations is still an open question.

This microscopic information points out a variety of further avenues of investigation. In the future, perhaps experiments will be performed that can directly explore some of the microscopic observations we have made thus far. With that in mind, we have made an effort to focus on behavior of the simulated system that may be physically relevant. To make connections with experimental data available today, we have to directly use macroscopic results, or use additional models in an effort to move from microscopic simulation results to measurements made in experiments. This is the subject of the next chapter.

Chapter 4

Silicon Indentation II

Direct comparison of our simulation results with available experimental data is a crucial aspect of our study. Where our simulations reproduce macroscopic experimental curves, we can use our results to try to obtain a microscopic explanation for the observed behavior.

Our primary focus is comparing our simulated load vs. displacement and load vs. resistance curves with available experimental data. Comparison between the results obtained by Weppelmann, *et al.* [1] is particularly rewarding because they used a spherical indenter. As a result, we can delineate some of the weak spots of our simulation method, and we can describe a set of experiments that may help settle an open question about the physical system. Comparing with the experimental load vs. resistance curves requires formulating a simple model to link information about the geometry of the transformed region in the simulation to macroscopic resistance. We find with the aid of this simple model that agreement with experiment is satisfactory, and with that we can better understand which physical characteristics of the system influence the electrical behavior under load.

Simulated load vs. displacement curves can be compared with the experiments of Weppelmann, *el al.* [1]. The experimental results shown in Fig. 4.1 used a spherical indenter of radius 8.5 μm. The simulation contains no absolute length scale, so results are

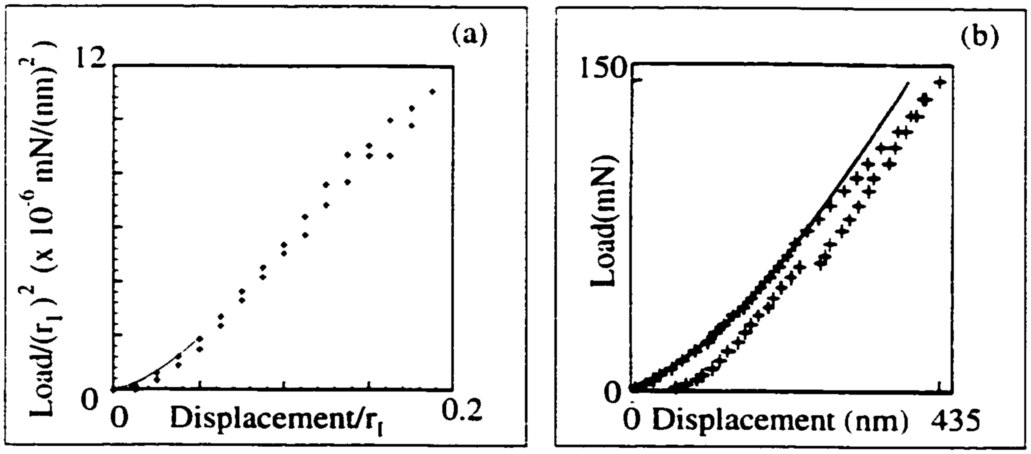

Figure 4.1: A comparison of the load vs. displacement curves for indentation on the (100) surface of Si: (a) simulation: (b) and experiment (taken from Ref. [1]). The solid line in each is a fit to the elastic solution.

scaled by the indenter radius, r_I. These are indentations with displacements smaller than in the simulations discussed in the previous chapter (see Fig. 3.6, for example). Here, in both simulation and experiment, unloading begins soon after transformed phases first appear underneath the indenter. In both curves, upon initial loading there is an elastic regime, where the load varies as the 3/2 power of the indentation depth [47], as indicated by the solid lines. Deviation from elastic behavior occurs at higher loads, as phase transformations begin to occur underneath the indenter. Finally, both curves exhibit a step in the unloading part, followed by a smooth decline to an unloaded state with residual plastic deformation. In the simulation, this residual deformation is due to finite elements that remain in a metallic phase.

There are some differences in the behavior of the simulated and experimental systems. When the simulation is scaled to the experimental indenter radius the initial transformation occurs at a displacement of 1200 nm, significantly deeper than in experiment. Certainly one cause for the late transformation in the simulation is that the smallest unit that can transform is a single finite element. Scaled to the experimental length scale, the size of a finite element is roughly 1 μm. In the experiment, transformations can occur on a length scale determined by a balance between volume energy gain and interface energy penalty according to Eq. 2.10. This length scale is on the order of 10 nm.

Another difference between simulation and experiment is that in experiment the phases deduced to have formed underneath the indenter are β-Sn upon loading, and the more complex phases bc8, r8, and hexagonal diamond upon unloading [1, 9, 10]; Fig. 4.2 indicates that in the simulation the observed phases are bct5 and the simple cubic phase, which forms in small amounts toward the end of the unloading cycle. These discrepancies between simulation and experiment can be attributed to shortcomings in the SW potential, and to the restriction to a two-atom unit cell in the simulations. The latter restriction, as mentioned earlier, can be relaxed by using a larger unit cell.

It is interesting that despite these differences, the simulation faithfully reproduces

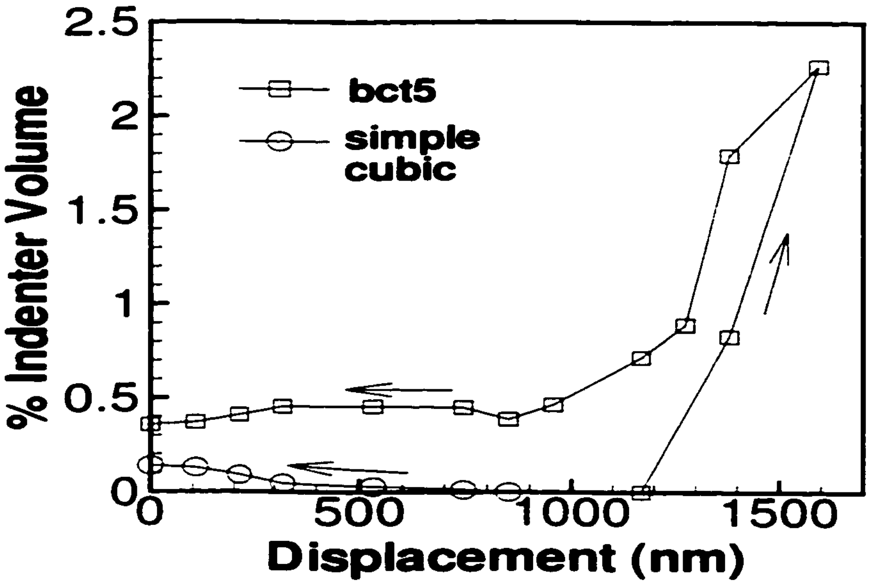

Figure 4.2: Amount of transformed phases as a function of indentation depth, expresses as a percentage of the total volume of the spherical indenter.

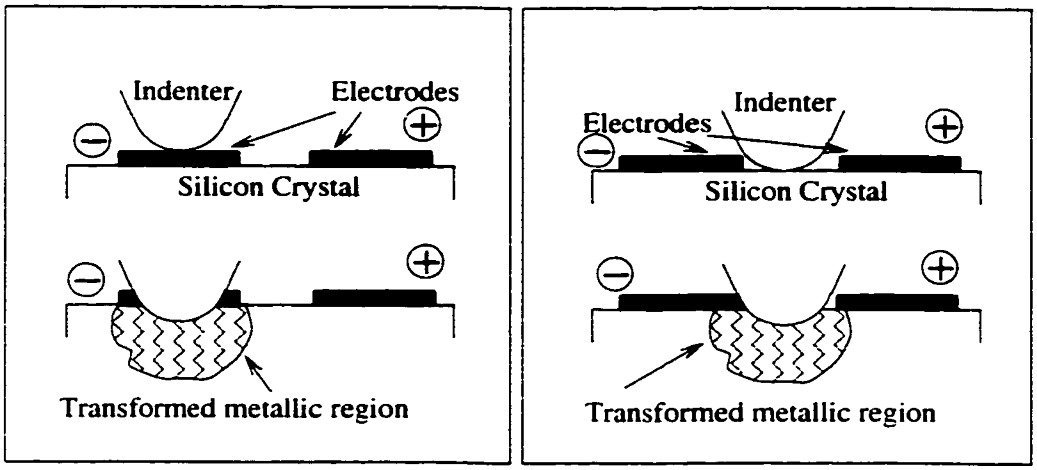

Figure 4.3: Schematic of experimental setup for indenting on and between electrodes.

the qualitative features of the experimental load vs. displacement curve, including the step upon unloading. In interpreting their experimental results, Weppelmann *et al.* assumed that at this step in the unloading curve one phase transforms into another completely [1, 9]. Our results indicate that although the step is associated with a large phase transformation, the number of transformed finite elements continues to change throughout the unloading part of the simulation.

Another macroscopic probe that experimentalists have used to gain insight into the behavior of indented silicon are resistance measurements. As metallic phases appear underneath the indenter, the resistance between a pair of electrodes on the surface of the sample can change. The connection between the appearance of metallic phases and the change in the macroscopic resistance is very complicated, but we have developed a simple model that captures the basic physics and enables us to connect our simulation results with experimental measurements.

We will focus on two types of resistance experiments that have been performed by Pharr *et al.* [3], shown schematically in Fig. 4.3. In both, two electrodes are placed on the surface of the silicon sample, and a voltage difference is applied between them. In one experiment, the indenter is directly on top of one of the electrodes; in the other, the indenter is between the two electrodes, slightly offset towards the negative one. Mann *et al.* used an experimental set up where the indenter itself served as one of the electrodes; but due to some of the details of the configuration they used, and the limitations of our simulation, comparison between their results and our simulation is difficult.

In the experiments of Pharr *et al.*, indentation and the resultant metalization underneath the indenter reduces the resistance from the background (R_b) to the measured (R_m) value. Before indentation, the resistance at each of the electrodes is determined by the Schottky barrier that forms at the metal-semiconductor interface [3], and the spreading resistance [48]. Physically, the spreading resistance is due to the current being forced through a bottleneck just beyond the electrode, before the current can spread through a larger region of the material further away from the electrode. The Schottky barrier and spreading resistance are local to each electrode, so we consider the resistances of the positive and negative electrodes to add in series: $R_b = R_b^{(+)} + R_b^{(-)}$.

As indentation proceeds, clusters of metallic-phase elements form underneath the indenter. When a cluster touches an electrode, current flows through the cluster and changes the measured resistance. We take the resistance of a transformed region, R_t, to be in parallel with the electrode's background resistance. This is a reasonable approximation. Current that completes the circuit via the background network will not be significantly perturbed by the indented region, whose dimensions are extremely small compared to the size of the electrode network (Fig. 2 in Ref. [3] indicates that the electrode network is about two orders of magnitude larger than the indenter); conversely, the resistance experienced by the current that passes through the indentation region will depend primarily on the local geometry of the transformed region. The metallic clusters that form upon loading are roughly hemispherical. Neglecting the influence of the electrode network, by dimensional analysis the spreading resistance of a metal hemisphere of radius a embedded in the surface of a semi-infinite sample of silicon is proportional to the resistivity of the silicon, ρ, and inversely proportional to a. By a simple electrostatic argument the constant of proportionality is $1/2\pi$ [48], giving us an estimate of $R_t \approx \rho/2\pi a$. If a metallic cluster touches both electrodes, then the circuit is shorted. With these approximations we arrive at

$$R_m = \begin{cases} 0 & \text{if short circuit} \\ \dfrac{\rho R_b^{(-)}}{2\pi a^{(-)} R_b^{(-)} + \rho} + \dfrac{\rho R_b^{(+)}}{2\pi a^{(+)} R_b^{(+)} + \rho} & \text{otherwise} \end{cases} \tag{4.1}$$

where $a^{(-)}$ and $a^{(+)}$ are the size of the clusters of metallic-phase elements in contact with the negative and positive electrode, respectively. Occasionally, more than one cluster will be in contact with an electrode, and in those cases we use the largest. As our definition of what constitutes a conducting cluster, we assume that only metallic elements fully surrounded by other metallic elements conduct. [1]

Within this model, at each electrode there is a crossover size for a transformed cluster: $a_c^{(-,+)} = \rho/\beta R_b^{(-,+)}$. For clusters of size much less than a_c, measured resistance is close to the background resistance; for clusters much larger than a_c, measured resistance goes as $1/a$. So when there is not a short circuit, we can write

$$R_m = R_b^{(-)} \left[1 + \frac{a^{(-)}}{a_c^{(-)}}\right]^{-1} + R_b^{(+)} \left[1 + \frac{a^{(+)}}{a_c^{(+)}}\right]^{-1} \tag{4.2}$$

First we consider low-load spherical indentations directly on the negative electrode, using the simulation data that produced Fig. 4.1(a). Simulated load vs. resistance curves are shown in Fig 4.4. In experiments with the spherical indenter, the silicon sample had a resistivity $\rho \approx .05$ Ωcm [1], but no data was given for the background resistance. To cover the widest range of reasonable R_b values, we plot curves for values of a_c/r_I ranging from 1.8 down to 0.0018, where r_I is the indenter radius; the highest value of a_c/r_I corresponds to a value $R_b^{(-)} \approx 5\Omega$, and the smallest to $R_b^{(-)} \approx 5000\Omega$. The predicted behavior could be checked by experiments where the indenter radius is varied; such experiments

---

[1] Another reasonable assumption, that all connected metallic elements make up a conducting cluster leads to the formation upon unloading of tenuously connected clusters, with some connections only an element or two thick (see Sec. 3.4.2). These connections do not appear stable with respect a decrease in the spacing of the mesh (see Fig. 3.8 and the accompanying discussion). Moreover, in regions where metallic and diamond phases are adjacent, the validity of the local approximation is suspect, so it is unclear what level of conductivity to assign these regions. It is not clear to us at this juncture how to model the conductivity of these tenuously connected clusters.

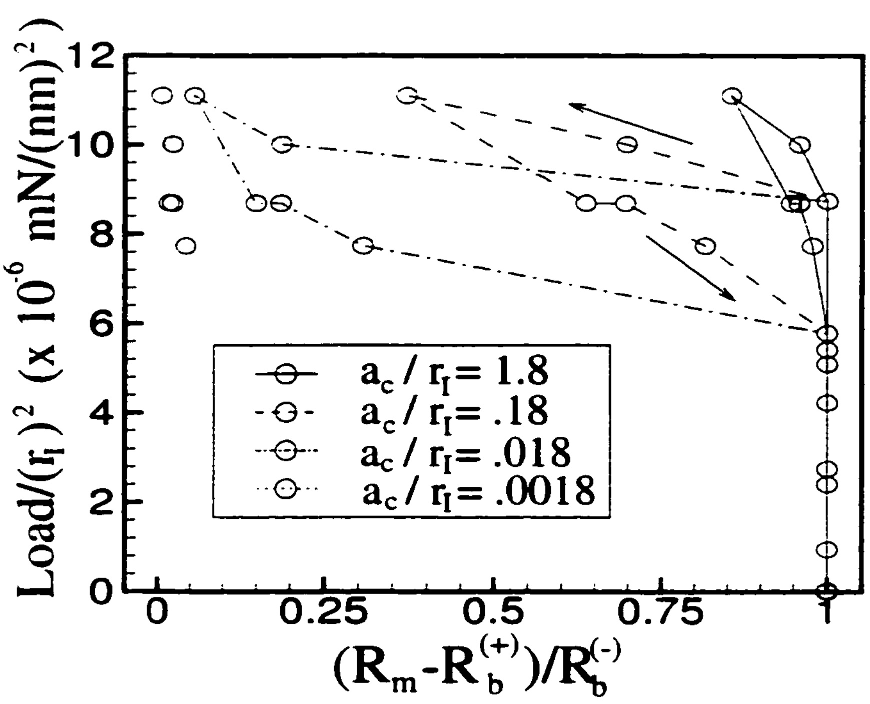

Figure 4.4: Load vs. resistance curves for indentation on an electrode with an indenter of radius r_I, for different values of a_c/r_I. The maximum indentation depth is $0.19r_I$.

would shed light on the nature of the reverse transformation upon unloading. In the simulations, where the large metallic cluster at maximum load gradually fragments and partially transforms back to the diamond phase upon unloading, the resistivity increases smoothly during unloading, especially for the mid-range values of a_c/r_I. If the entire transformation were to occur at the step in the load vs. displacement curve in Fig. 4.1, as surmised by Weppelmann *et al.* [1, 9], during unloading the resistance would be constant except for a sudden change at the step.

It is worthwhile to note that the recent resistance measurements of Mann *et al.* do exhibit continuous change in the resistance upon unloading, but a Berkovich indenter is used instead of a spherical indenter [11]. The change of indenter can make comparison between the two experiments difficult, for this change can affect macroscopic features substantially. For example, for small loads, the load vs. displacement curves obtained by Mann *et al.* do not exhibit a discontinuity upon unloading, unlike what is observed by Weppelmann *et al.* as shown in Fig. 4.1.

Unfortunately, it is difficult to meaningly compare our simulation results with the resistance curves obtained by Mann *et al.*. In their experiments, the indenter itself is metal and serves as one of the electrodes. The indenter must push through a native oxide layer of the silicon, and it is this layer that dominates the resistance measurements upon loading. The data is presented in such a way that the huge drop in resistance that occurs when the oxide layer is pierced makes subsequent changes in resistivity due to the growth of the metallic cluster difficult to observe. Interesting behavior is evident upon unloading in their measurements, but it is attributed to differences in resistivity between the various phases, something our simple model cannot capture.

Next we consider deeper simulated indentations. These results are qualitatively different than high-load experiments using spherical indenters[9] presumably because significant cracking is observed in the experiments, while the formation of cracks was not included in the present simulations. However, the simulation results are similar to the

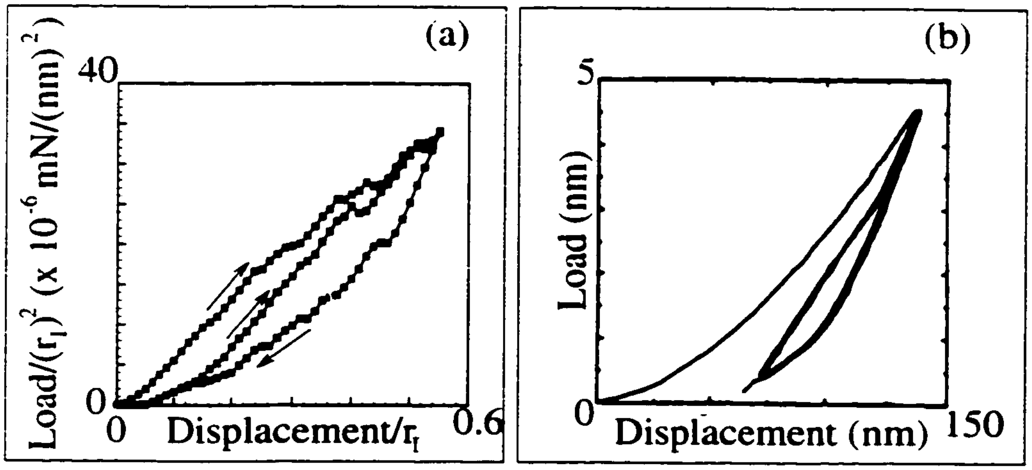

Figure 4.5: A simulated load vs. displacement curve for a deep indentation (a) and an experimental curve taken from Ref. [2] (b). Additional simulations with a coarser mesh show that the hysteretic loop is reproducible (see Fig. 3.5).

low-load Berkovich indenter load vs. dispacement curves [2, 3], where cracking does not occur. In particular, both have a reproducible hysteretic loop, as shown if Fig. 4.5. The same experiments also provide load vs. resistance measurements [3]. These results present a further opportunity to test the validity of the simulation and the simple electrical model presented above.

To compare the simulated load vs. resistance curves with the experimental curves we use the experimentally determined values for the constants in Eq. (4.2): $\rho \approx 10$ Ωcm, $R_b^{(+)} \approx 5$ kΩ. The total background resistance R_b varies from one experiment to the next; $R_b^{(-)}$ is chosen to ensure that $R_b = R_b^{(+)} + R_b^{(-)}$ is equal to the experimentally measured total background resistance. With these parameters, $a_c \approx 1\mu$m, which is the approximate size of the indentations in the experiments. Had the indentations been significantly smaller, they would not have affected the measured resistance; had they been significantly larger, a smooth change in resistance as a function of indentation depth would have been difficult to observe (these two extremes of behavior are visible in Fig. 4.4 for the largest and smallest values of a_c/r_I). Using these constants in Eq. (4.2), we obtain the simulated resistance curves shown in Fig. 4.6. The simulation data was scaled to a maximum indentation depth that matches that of the corresponding experimental curves, also shown in Fig. 4.6. The simulated curves reproduce well the qualitative features of the experimental results. Given the shortcomings of the Stillinger- Weber potential used in the present calculations, this qualitative agreement suggests that the basic features of the resistance measurements are insensitive to the details of the microscopic energy surface and the indenter geometry in the absence of cracking.

We have simulated resistance and load vs. displacement curves; the results reproduce qualitatively available experimental data. In the course of comparing simulation and experiment we have discussed several open issues and possible future work that would help clarify the behavior of silicon during indentation. For example, experimental resistance measurements for spherical indenters of varying radii would help determine whether the

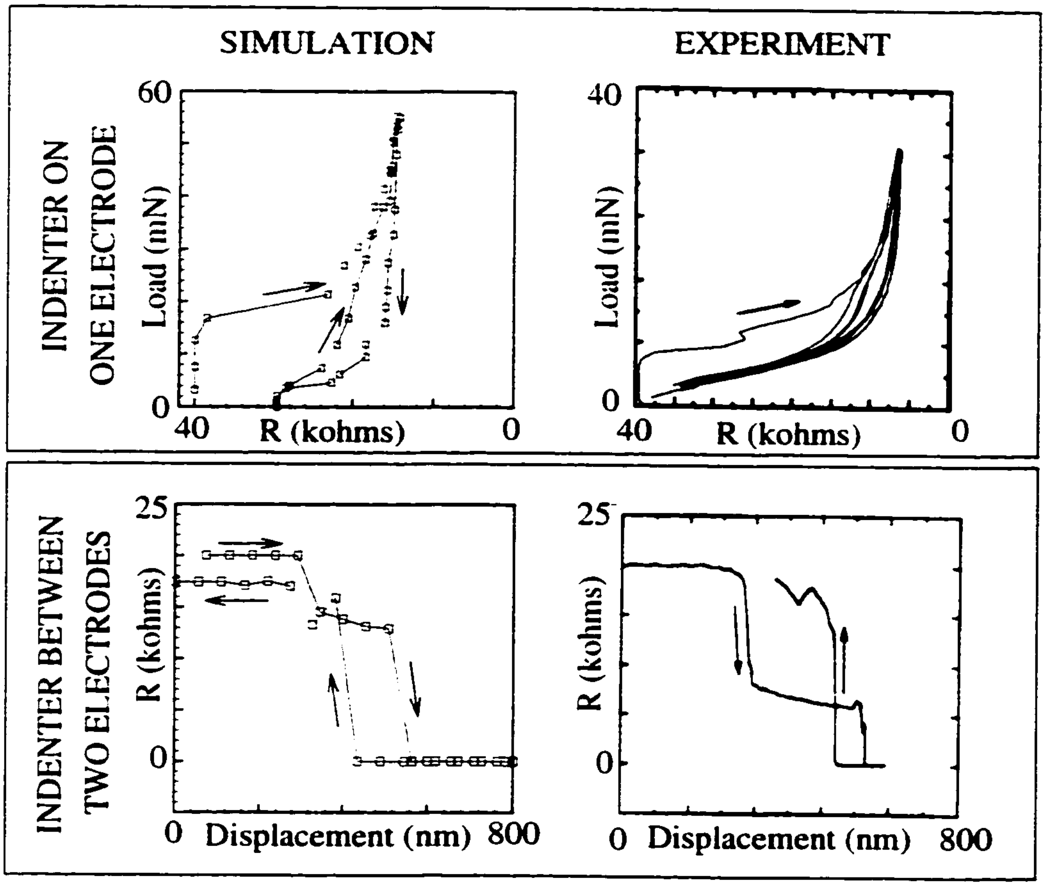

Figure 4.6: Comparison of experimental and high-load simulated resistance curves for the two different experimental geometries shown if Fig. 4.3. The experimental curves are taken from Ref. [3].

reverse transformation upon unloading occurs suddenly or gradually. In all simulations we used a spherical indenter. but similarities were noted between the deeper simulated indentation results and Berkovich indenter experiments: further work is needed to understand how factors such as indenter shape and cracking in the indented region influence whether macroscopic curves exhibit a step or reproducible hysteretic loop.

Chapter 5

Indentation of $PbTiO_3$

This chapter focuses on indentation of $PbTiO_3$. In some respects this system is much like silicon indentation. In particular, both have a multi-welled microscopic energy surface that makes behavior of the system potentially very complicated. But the details of this microscopic energy surface–such as the positions and distances in configuration space between the local minima–are very different, which gives rise to qualitatively different macroscopic behavior.

As in the previous chapters, our primary tool used to investigate indentation of $PbTiO_3$ will be the local quasicontinuum method, extended to handle a complex Bravias lattice. Unfortunately, here there is much less experimental guidance than for silicon indentation. We will attempt to connect with experiment where possible, but our primary goal will be to explore the physics of piezoelectric indentation. We pay particular attention to the connection between the microscopic energy surface of $PbTiO_3$ and macroscopic measures in both the linear elastic regime and for deeper indentations. A question we will always keep in mind: if there are dramatic things happening on the microscopic scale, will they be macroscopically observable like in silicon? We point out several features our results that are surprising, some of which call into question the conventional microscopic picture of how piezoelectrics behave that underlies some theoretical models.

For $PbTiO_3$ we will not focus on issues of dependence on potential, since we have no other suitable potential available for comparison. Also, though we have thoroughly studied the convergence properties of our simulations of indented $PbTiO_3$ to settle on our finite element mesh, we will not describe these studies here. They are not particularly enlightening.

5.1 Previous Work

Indentation studies of piezoelectrics are not as extensive as those done for silicon, perhaps in part because no unusual behavior such as hysteretic load vs. displacement curves have been observed. Bahr *et al.* used indentation to study the elastic, cracking, and delamination properties of PZT thin films for MEMS applications (PZT is a solid solution of $PbTiO_3$ and $PbZrO_3$) [21]. Others have used indentation to study the failure behavior of piezoelectrics [49]. But in these studies indentation is used as a tool to produce cracks or delamination, not to carefully probe the high-pressure behavior of the material. Ramamurty *et al.* has performed detailed indentation experiments on piezoelectrics, but have confined their experiments to shallow indentation depths in the linear elastic regime [4].

Detailed studies of indentation of piezoelectrics like that of Ramamurty *et al.*, but for large indentation depths and/or large electric fields are not available in the literature. Such studies would be interesting because they would probe some the fundamental behaviors of piezoelectric materials in the nonlinear regime. How do external electric fields affect the macroscopic load vs. displacement curves? How do external electric fields affect the evolution of the polarization field inside the material during indentation? And what happens if indentation penetrates deeper into the sample? Does switching occur, and if so, how and at what penetration depth? Is there a macroscopic signature that can be observed as switching occurs?

There is already a large body of computational and theoretical work on piezoelectric materials, using a variety of methods. Calculations based on density functional theory (DFT) have been very successful in providing quantitative information about the microscopic behavior of piezoelectrics, including domain wall energies, elastic constants, and dielectric and piezoelectric coefficients [50]. However, DFT calculations are computationally intensive, and as a result can only be used to study perfect crystals in the presence of uniform stress and polarization fields.

Finite element methods have also been used to model piezoelectric materials, and have the advantage of being able to track nonuniform stress, electric, and polarization fields throughout a system. This is crucial for modelling indentation, and useful in general for modelling the electromechanical behavior of piezoelectric materials in nanosystems. However, a finite element simulation is only as accurate as the underlying constitutive relation. In the linear regime, where it is possible to formulate a good constitutive relation, finite element techniques successfully reproduce theoretical and experimental results [26]. However, developing a constitutive relation that incorporates nonlinear behavior such as switching has been extremely challenging.

Significant progress in developing such a constitutive relation has been made using micromechanical modelling. By using a set of reasonable equations to describe the microscopic behavior of a piezoelectric, then averaging over microscopic domains to obtain microscopic response, several groups have been able to reproduce some experimental results [51, 52]. However, all present work requires both a uniform stress and electric field, only switching between tetragonal phases is considered, and the criterion used to determine when switching occurs is phenomenologically based.

5.2 Simulation Details

The general setup of the mesh and coordinate system is the same as that for three dimensional simulations of silicon indentation, shown in Fig. 3.4. The ratio of the minimum mesh spacing to indenter radius, however, is smaller for the $PbTiO_3$ simulations.

This was done to ensure the results were converged with respect to mesh spacing, especially very close to the indenter. For $PbTiO_3$ the ratio is about 1/50.

The five atom primitive unit cell of $PbTiO_3$ is taken to be the unit cell used in the quasicontinuum method (see Fig. 2.3). With the simplifications described in Sec. 2.3.3, this means there are three degrees of freedom per unit cell. In all the simulations, the initial uniform polarization is in the positive z direction. Single crystal $PbTiO_3$ is used in the simulations, with the crystallographic directions [100] along the x-axis, [010] along the y axis, and [001] along the z axis.

The indenter is modelled here the same way as for the three-dimensional silicon indentations (see Eq. 3.1). For convenience we reproduce the equation here. The total energy that is minimized is a sum of the strain energy of the finite element mesh, U_M and the energy due to the indenter [46],

$$U_{Tot} = U_M + \frac{\alpha}{2}\sum_j \left(\frac{r_I - |\vec{r}_I - \vec{r}_j|}{r_I}\right)^n \theta(r_I - |\vec{r}_I - \vec{r}_j|) \tag{5.1}$$

where θ is the Heavyside step function, r_I is the indenter radius, and $\vec{r}_I$ and $\vec{r}_j$ are the position vectors of the center of the indenter and the node j of the finite element mesh, respectively.

Unlike the case for silicon, there is enough experimental information on the configuration of the indenter to enable us to model it in the simulation. We choose $n = 2$ to mimic elastic behavior. We take α to be proportional to E, the Young's Modulus of the experimental indenter; α must also be proportional to a, the area of a finite element face. Noting that the experimental indenter is hemispherical with the flat face mounted on metal plate (see Fig. 2 in Ref. [4]), there is only one length scale, r_I. By dimensional analysis we arrive at $\alpha \propto Ear_I$. For convenience we set $\alpha = Ear_I$. These values of n and α would be strictly correct if the indenter were made up of a collection of independent springs of length r_I aligned along the z-axis, with one end of each spring is attached to a node, and the other is fixed to a plane parallel to the surface of the sample and through the center of the indenter. This approximation is closest to being correct for indentations very shallow compared to the indenter radius.

Determining when switching occurs (when one phase transforms into another) underneath the indenter is somewhat trickier than with silicon. There, the phase of a finite element was determined by letting the unit cell of silicon relax without constraints, with the beginning configuration dictated by the deformation gradient and degree of freedom position of the particular finite element. With $PbTiO_3$ that is not possible because some of the phases we encounter are unstable without applied pressure. As a result, we must identify when switching occurs *in-situ* by noting the position of the polarization. As discussed in Sec. 2.3.3, the tetragonal phase has polarization in one of the $< 100 >$ directions, the orthorhombic phase has polarization in one of the $< 110 >$ directions, and the rhombohedral phase has polarization in one of the $< 111 >$ directions.

The electric field couples linearly with the strain in a piezoelectric, and this necessitates defining the electrical boundary conditions of the system. We take the electric field to be constant throughout the sample during the indentation process. Physically, this corresponds to free charge carriers compensating for accumulated bound charge that forms as a result of the polarization gradients that develop in the course of indentation. This does not correspond to the experimental situation, but serves as a simple way to begin exploring the effect of external electric fields on the simulated system.

5.3 Low-load Indentations

The low-load simulated load vs. displacement curves for different electric fields are shown in Fig. 5.1(a). All the indentations are done at 300K, though setting the temperature to 0 K made only a very small difference in the curves (about 4% increase in the load). [1] The experimental results are shown in Fig. 5.1(b) for a room temperature indentation with an indenter of radius .8 mm [4]. The magnitude of the simulated and

---

[1] The temperature is included only via the mean-field theory approximation in the free energy expansion of $PbTiO_3$ discussed in Sec. 2.3.3. The free energy is minimized via a conjugate gradient algorithm, as with silicon. There is no microscopic temperature or dynamics.

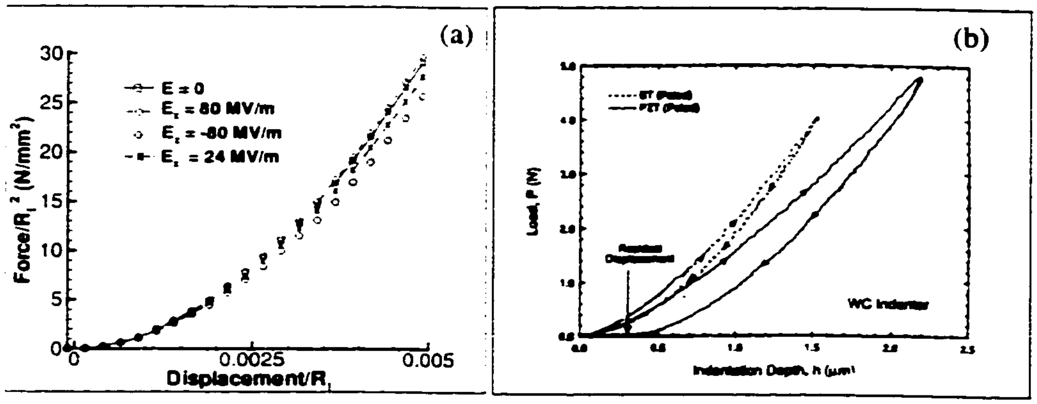

Figure 5.1: Simulated load vs. displacement curves for $PbTiO_3$ for several electric fields (a), and an experimental curve for PZT in the absence of an electric field (b). The experimental results were taken from Ref. [4].

experimental load vs. displacement curves are within 20% of each other, which is fortuitous agreement given the crudeness of the simulated indenter, and that the experimental results are for PZT, not $PbTiO_3$.

In Fig. 5.1(a), electric fields in the x and z directions are applied with magnitudes about 80% of the magnitude that would induce a 90° or 180° switch, respectively. In all the simulations at these low loads, no switching was observed. When the electric field is directed along the x-axis, the material becomes easier to indent in the simulation because the electric field breaks the symmetry and the material shears as the indenter advances (recall that the indenter is frictionless)

There is a large asymmetry in the load vs. displacement curve with respect to electric field direction along the z axis. Directing a strong electric field with the initial polarization has little effect, while an electric field directed opposite the initial polarization softens the material significantly. We can determine the fundamental microscopic source of this asymmetry by examining the effective Hamiltonian that serves as the foundation of our method. The frequencies of the phonons that may be relevant to the asymmetry can be calculated from the effective Hamiltonian in Eq. 2.40. The frequency of one family of phonons in particular changes substantially as the electric field goes from a large positive

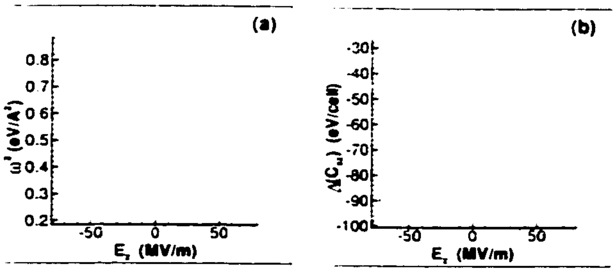

Figure 5.2: A plot of ω_x^2, the frequency squared of the phonon that displaces the polarization in the x-direction (a), and ΔC_{xz}, the correction to the diagonal elastic constants (b). Both are plotted with respect to the electric field in the z-direction. Plots for ω_y^2 and ΔC_{yz} are identical.

value to a large negative value along the z-axis, as indicated in Fig. 5.2 (a). These are the phonons that move the polarization in the xy plane, the plane perpendicular to its initial direction. When the frequency of these phonons becomes smaller, that means that the restoring force is becoming weaker, so it becomes easier to rotate the polarization vector away from its initial direction. In other words, switching to another polarization direction becomes increasingly favorable.

Changes in the frequency of the phonons shown in Fig. 5.2 (a) can be linked to changes in the elastic constants of the material. For a complex material one can define raw elastic constants, which are the elastic constants when the internal degrees of freedom are frozen. Each physical elastic constant is then the sum of a raw elastic constant and corrections due to relaxation of internal degrees of freedom. One can show from Eq. 2.40 that

$$\Delta C_{xz} = -\frac{L_{x,xz}^2}{\omega_x^2} \tag{5.2}$$

where ΔC_{xz} is a correction term for the diagonal elastic constant C_{xz}, L is the coupling between components of strain and the internal degrees of freedom. [2] and ω_x^2 is the frequency squared of the phonon that displaces the polarization vector in the x-direction. C_{xz} and

---

[2] In Eq. 2.40 there is not linear coupling between strain and internal degrees of freedom, because of the cubic symmetry of the reference state. However, when Eq. 2.40 is expanded about one of the tetragonal wells, it does have such a term, and that is what we refer to with "$L_{x,xz}$"

C_{yz} in particular are highly asymmetric with respect to electric field direction, since they have a $1/\omega^2$ dependence on phonons that soften significantly (see Fig. 5.2 (b)). This gives rise to the asymmetry in the elastic response of the system. Thus the asymmetry observed in the load vs. displacement curve in Fig. 5.1 is a macroscopic manifestation of the asymmetry of the behavior of certain phonons with respect to the direction of the electric field.

It is also interesting to note that it is the shear elastic constants that are affected by the electric field, while C_{xx}, C_{yy}, and C_{zz} are relatively insensitive. So when an electric field becomes strong enough to induce a switch, the material does not begin the switch by becoming very soft and compressible in the direction of the electric field; rather, the material becomes unstable with respect to shears. Moreover, the type of phonons that become soft indicate that when the switch begins the PbTiO$_3$ unit cell is heading toward a 90° switch, not a 180° switch. This meshes well with the results of elastic band calculations that indicate that the lowest energy path for a 180° switch due to an electric field is actually a combination of two 90° switches [53].

In the simulations in Fig. 5.1, there is no hysteresis observed during unloading. There is, however, hysteresis in the experimental curve, which could be caused by the formation of cracks defects, or by switching in regions of the piezoelectric. Since switching does not occur in the simulations at these low loads, hysteresis in the experiment is likely due to the formation of cracks or defects. These cannot form in the simulation (see discussion in Sec. 2.2).

5.4 High-Load Indentations

For indentation that is sufficiently deep, switching begins to occur. Fig. 5.3 shows the load vs. indentation depth and average polarization vs. indentation depth curves for these high-load indentations. For Figs. 5.3 (a) and (b) the total electric field is zero, and for Figs. 5.3 (c) and (d) the electric field is directed opposite the initial polarization. First we consider the case with no external electric field. then explore what happens with a strong electric field present.

5.4.1 Indentation in the Absence of an Applied Electric Field

The curves in Figs. 5.3 (a) and (b) are marked by their lack of distinctive features. The curves are smooth, and there is virtually no hysteresis. Yet if we observe the polarization pattern beneath the indenter. we find that switching has occurred.

Figs. 5.4 and 5.5 show slices of the finite element mesh in the xz plane the xy plane. respectively. In Fig. 5.4 the slice is at $y = 0$: the box in that figure marks the approximate z position of the slice in Fig. 5.5. Both slices are from the same simulation at an indentation depth of about $0.03r_f$. Clearly, many finite elements have moved significantly from their initial polarization state. In Fig. 5.4, there is a clear V-shaped central area where the polarization has rotated from its initial position by 90°. This area is separated by a domain wall several finite elements thick from finite elements that have not deviated substantially from their initial polarization state.

It is surprising that none of the transforming finite elements are close to a tetragonal phase. Fig. 5.5 indicates that their polarization has a significant component in one the $< 110 >$ directions. which is associated with the orthorhombic or rhombohedral phases. This is not a mesh effect; rotating the mesh about the z axis gives the same results. This is noteworthy because the tetragonal phase is the lowed in energy, and because micromechanical models only consider transformations between tetragonal phases [51, 52]. To better understand the evolution of the configuration of these finite elements we focus in on a two representative finite elements and follow their evolution as indentation proceeds.

The evolution of these representative finite elements are shown in Fig. 5.7. Their approximate positions are marked A and B in Fig. 5.4. For now we focus on Figs. 5.7 (a) and (b), which show the polarization vectors for the representative finite elements as a function of indentation depth in the absence of electric field.

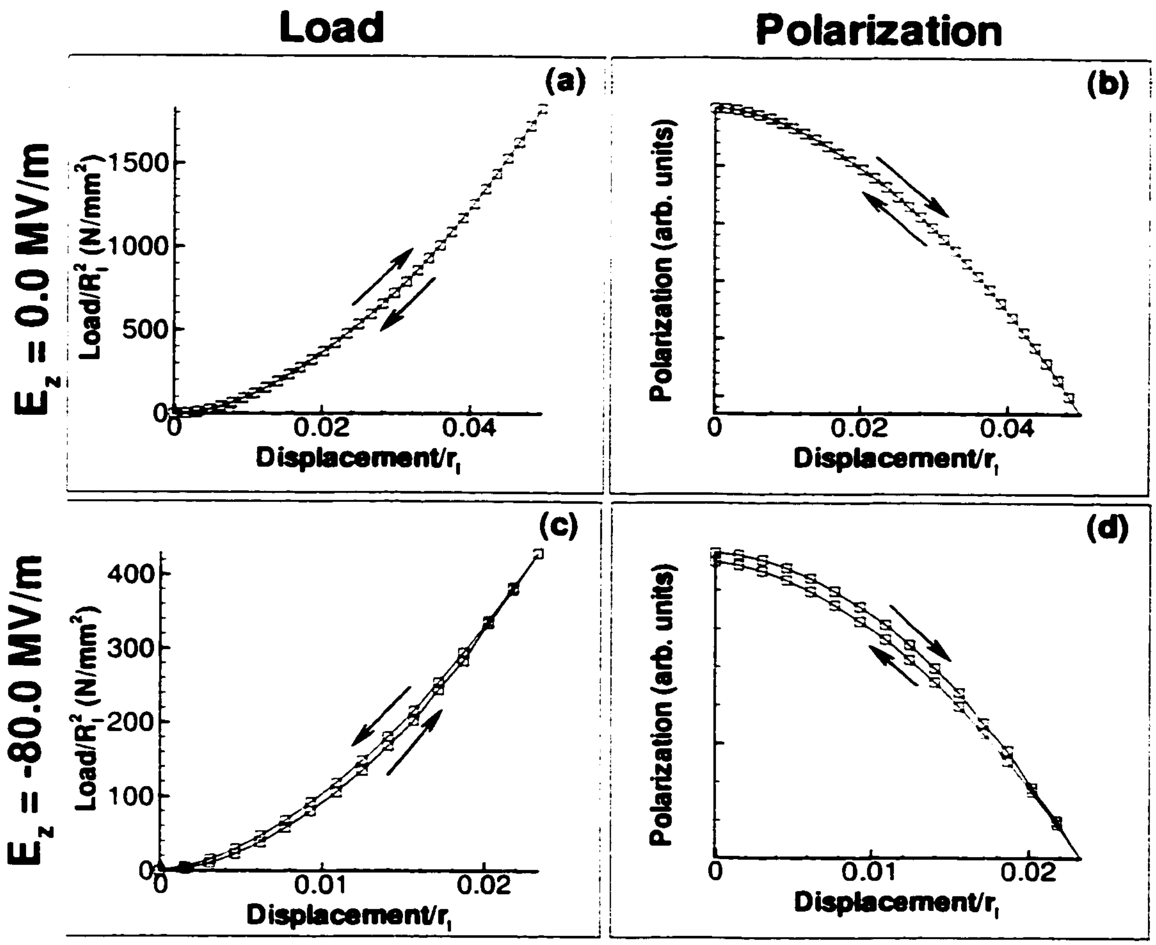

Figure 5.3: The load vs. displacement and average polarization vs. displacement curves for high load indentations. Results are shown for no electric field ((a) and (b)) and for a strong electric field in the negative z-direction ((c) and (d)).

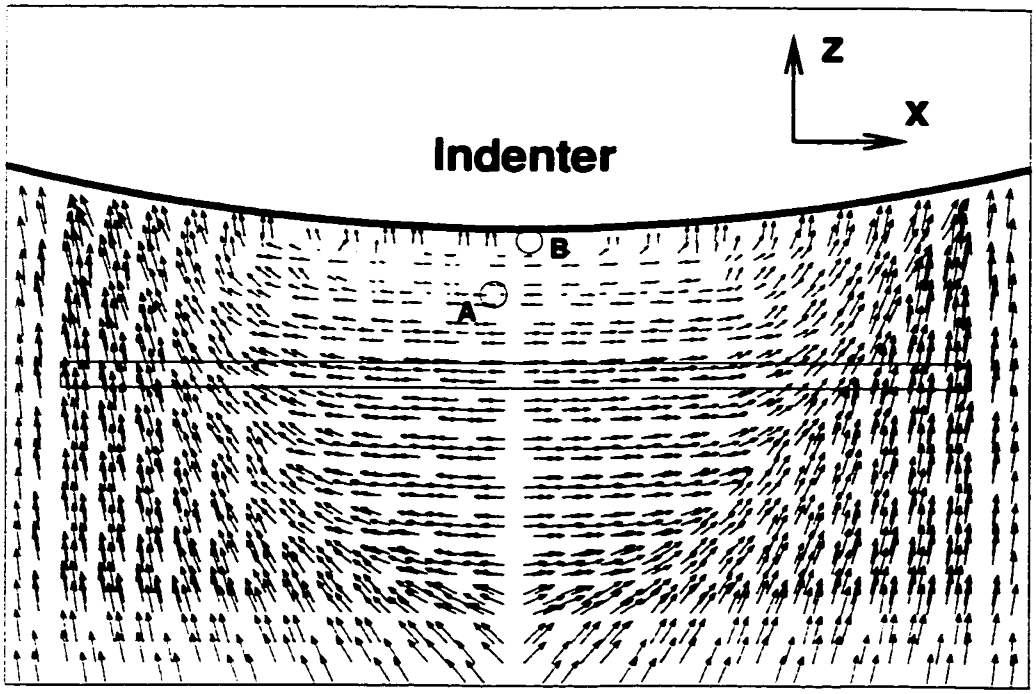

Figure 5.4: Slice through a close-up of the simulated system at $y = 0$. The arrows are polarization vectors of each of the finite elements. The box marks the approximate position of the slice that is shown in Fig. 5.5. The regions marked "A" and "B" indicate the approximate positions of the finite elements shown in Fig. 5.7.

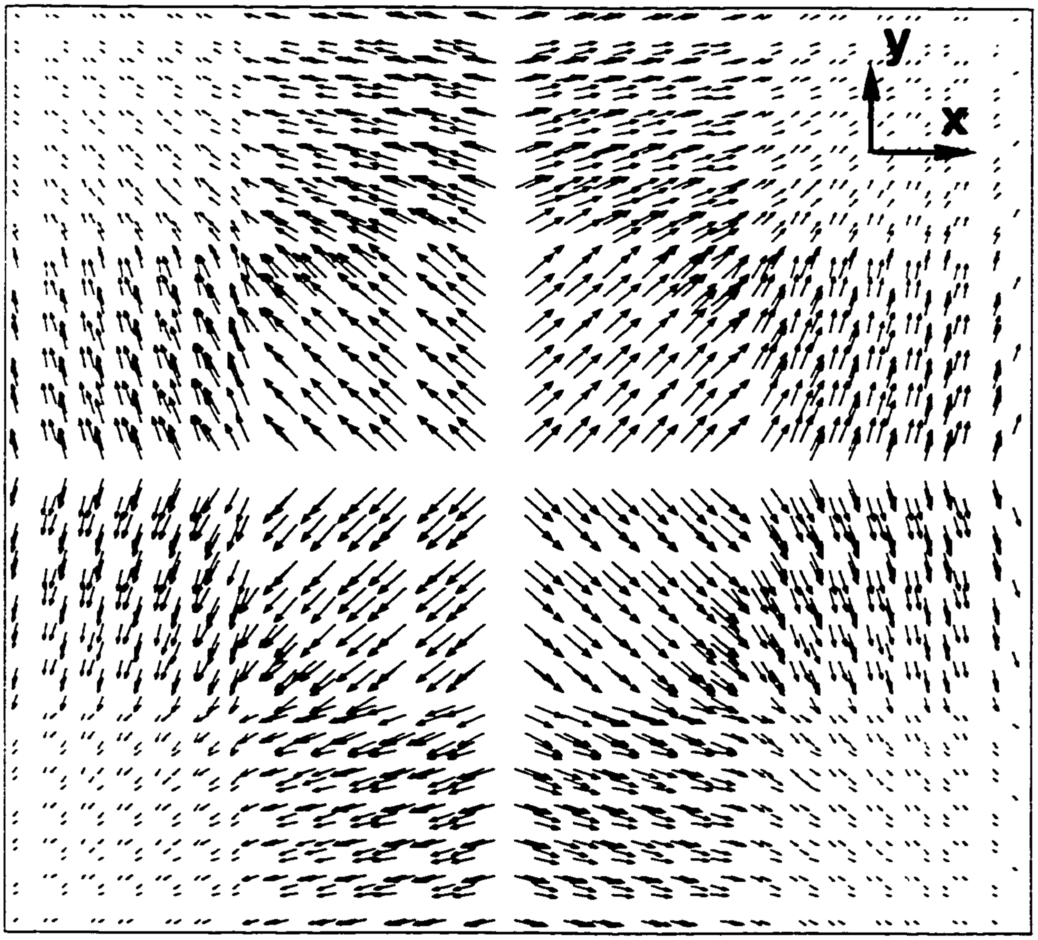

Figure 5.5: Slice through a close-up of the simulated system in the xy plane. The arrows are polarization vectors of each of the finite elements. The approximate position of the slice is marked by the box in Fig. 5.4. The scale is the same as in that figure.

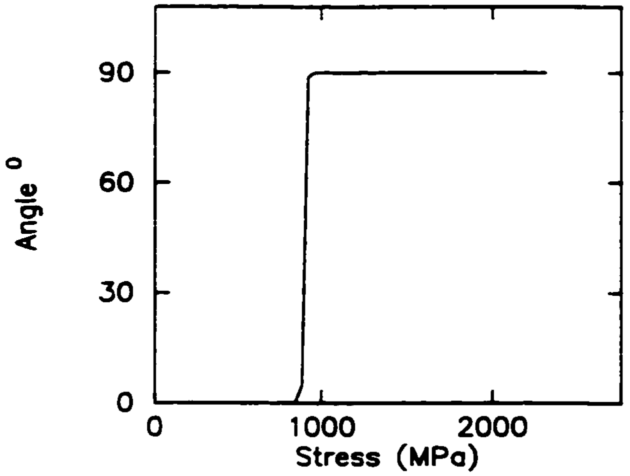

Figure 5.6: Polarization response of a single $PbTiO_3$ unit cell under compressive stress along the z axis. The polarization is initially in the z-direction, and ~~tan^{-1}~~$(p_{\perp}/p_z)$ is plotted along y-axis. $\tan^{-1}$

The polarization evolution in Figs. 5.7 (a) and (b) is completely different from the physical behavior usually associated with piezoelectric materials. Consider a poled piezoelectric unit cell with free boundary conditions. An applied stress field or external electric field of sufficient magnitude can be used to switch the polarization of the unit cell, and in general this switch occurs discontinuously. For example, uniform stress along the axis of polarization will cause a discontinuous 90° rotation of the polarization, as illustrated in Fig. 5.6. This simple physical picture of sudden jumps of polarization from one well-defined orientation to another is not only a convenient way to understand how these materials behave, but also serves as the basis for micromechanical theories used to study switching of piezoelectrics [51, 52]. Our simulations suggest that at least for the case of indentation, this picture does always capture the evolution of the polarization accurately.

In contrast to the picture of discontinuous jumps of polarization, we see in Fig. 5.7 (a) and (b) continuous evolution of the components of the polarization vector. In addition, there is no microscopic hysteresis: the evolution the polarization follows upon unloading is virtually the exact reverse of the path followed upon loading.[3] This microscopic reversibility gives rise to the macroscopic reversibility observed in Figs. 5.3 (a) and (b). Apparently the strong elastic coupling between neighboring regions of the material prevents the sudden change in unit cell shape that necessarily accompanies a discontinuous 90° switch, forcing the polarization to evolve continuously. An important caveat is that defects and cracks cannot form in the simulation; further work needs to be completed to determine how these structures may affect switching behavior.

The evolutions depicted in Figs. 5.7(a) and (b) both follow unexpected paths through configuration space. Finite element A moves from the initial tetragonal phase to a rhombohedral phase, where the magnitudes of the polarization components are approximately equal, at in indentation depth of about $0.02r_I$. Upon further indentation, the z component of the polarization disappears, while the x and y components remain equal in

---

[3] During unloading, the polarization of finite element B (Fig. 5.7(b)) follows a path rotated 180° relative to the path followed during loading, but these two paths are related by symmetry and give exactly the same energy and stress contribution to the system.

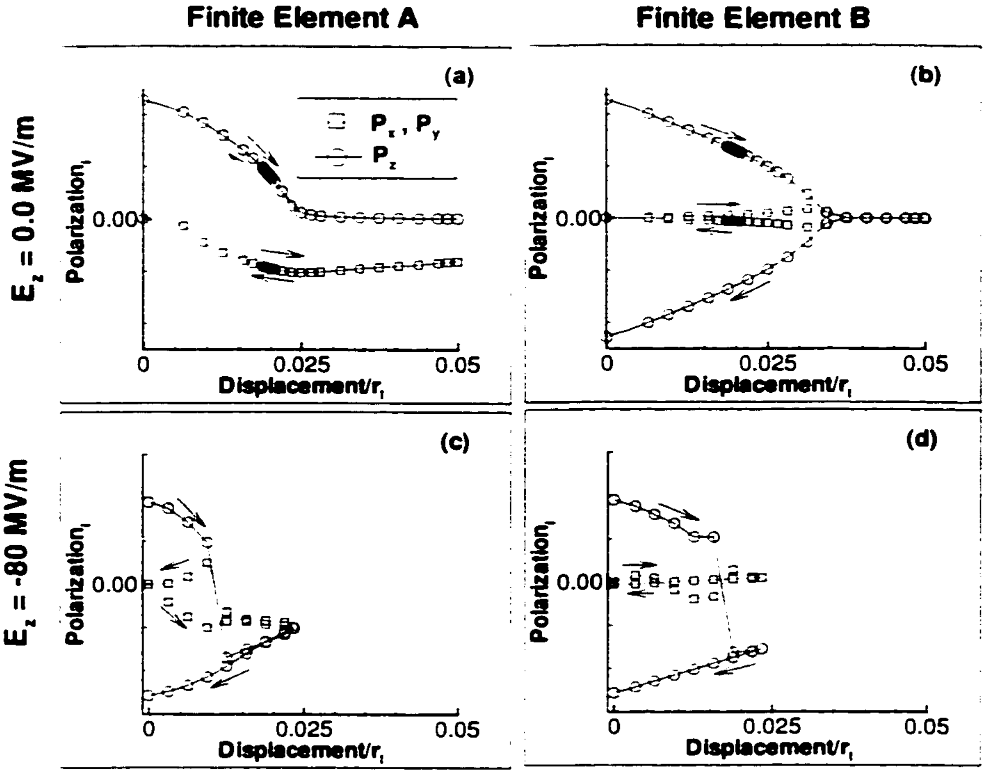

Figure 5.7: The polarization of two typical finite elements as a function of indenter depth. The components of the polarization vector are shown: the x and y components of the polarization are identical. The same two finite elements are tracked for zero electric field ((a) and (b)), and for a strong electric field in the negative z-direction ((c) and (d)). The approximate positions of the finite elements are labelled in Fig. 5.4

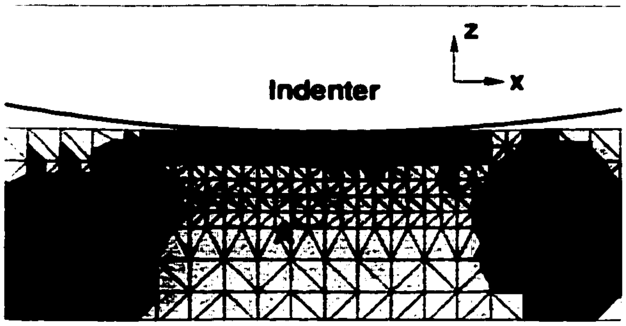

Figure 5.8: A close-up of the slice of the mesh shown in Fig. 3.4. Dark shading corresponds to negative values of ϵ_{xx}; lighter shading corresponds to positive values of ϵ_{xx}. The finite elements marked with "A" and "B" indicate the approximate position of the finite elements in Fig. 5.7.

magnitude and non-zero: this is the orthorhombic phase. In finite element B, the polarization, initially directed along the z-axis, shrinks and eventually disappears completely. This final state is the paraelectric phase, which has no intrinsic polarization and becomes stable at temperatures above 760K [39]; it becomes stable at lower temperatures at elevated hydrostatic pressure.

The reason for the different evolution of the two finite elements is evident from Fig. 5.8, which is a slice through the 3-d finite element mesh. The darker shading indicates a negative value of ϵ_{xx}, while the lighter shade indicates a positive value. Finite element B exhibits polarization evolution typical of finite elements closest to the indenter. Much as the concave surface of a bent rod is under compression, the finite elements closest to the indenter are under compression in the xy plane, preventing the x and y components of the polarization from becoming large. Finite element A is representative of finite elements slightly further away from the indenter, where the material is under tension in the xy plane. As a result, the polarization precisely aligned with the z-axis is not stable and it develops a component in the xy plane.

Other finite element may evolve at different rates than finite elements A and B, but all have polarization behavior qualitatively similar to that of either finite element A or finite element B. *None of the finite elements in the system transform into a tetragonal phase.* Finite element A is one of the first to move from its original tetragonal energy well. In general. we find that regions in the sample begin taking on rhombohedral character at an indentation depth of approximately $0.02r_I$: we define this as the onset of switching. [4]

5.4.2 Indentation in the Presence of an Applied Electric Field

When a large electric field is applied in the direction opposite the initial polarization. the microscopic and macroscopic behavior is very different than when there is no electric field. Figs. 5.3 (c) and (d) show the macroscopic load and average polarization as a function of displacement in the presence of an electric field with a magnitude about 80% of the switching field. As is the case in the absence of an electric field. the macroscopic curves are smooth; but now there is hysteresis. What is particularly striking is that in Fig. 5.3 (c), during unloading the load is *higher* than during loading. This is counterintuitive. One would expect residual deformation underneath an indenter to leave a dent in the surface, not a bulge.

This strange behavior can be explained by looking at Figs. 5.7 (c) and (d). In the presence of an electric field. all the finite elements that transform change into either an orthorhombic phase (like Fig. 5.7 (c)) or into a tetrahedral phase (like Fig. 5.7 (d)), and all transform with a jump in the polarization that aligns it with the electric field. The polarization remains aligned with the electric field even when the load is completely removed. Due to this hysteresis. at any point in the unloading curve. there are some finite elements with polarization lined up with the electric field that were not so oriented at the corresponding point in the loading part of the curve. These excess finite elements with polarization pointing with the electric field are evidenced by the hysteresis in the polarization curve in Fig. 5.3(c). These finite elements give rise to the increased load

---

[4] This should be considered a maximal value. The smallest region that can transform during a simulation is a single finite element. If the system were given the option of doing so. it would likely be more energetically favorable to transform sooner over smaller volumes, as long as bulk energy changes dominate interface energies. Reducing the grid spacing relative to the indenter radius does result in transformations occurring slightly earlier.

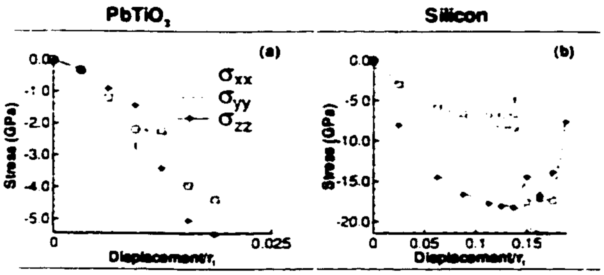

Figure 5.9: The stress for a single finite element as a function of indentation depth. for $PbTiO_3$ (a) and silicon (b). The arrows mark the point immediately before the internal degree of freedom changes position discontinuously. The finite element A from Fig. 5.7 is tracked in (a). and a finite element in roughly the same position in the silicon mesh is tracked in (b).

during the unloading cycle: when the polarization is against the electric field. as it is before indentation proceeds, the unit cell tends to be short and squat: when the polarization points with the electric field, the unit cell tends to be long and thin, pushing up against the indenter. So over a load/unload cycle, the piezoelectric does positive net work on the indenter. and the energy source is the external electric field.

It is also interesting to note that though there are jumps in the polarization in finite elements like those shown in Figs. 5.7 (c) and (d), the load vs. indentation depth curve remains smooth (see Fig. 5.3(c)). This can be explained simply by noting that though the polarization does change suddenly, the stresses experienced by finite element remain fairly smooth. In Fig. 5.9 (a) the diagonal stress components for finite element A (see Fig. 5.7) are shown as a function of indentation depth. The arrow marks the point immediately before the polarization shifts discontinuously. Though the jump of the polarization vector illustrated in Fig. 5.7(c) is fairly dramatic, the stress of that finite element remains smooth. However, for $PbTiO_3$ a switch of the polarization vector involves atomic displacements on the order of .1 Å, a relatively small perturbation. Compare this shift to that of silicon, where shifts in atomic displacement during phase transformations can be larger by an order of magnitude. As a result the stress of a silicon finite element that undergoes a phase transformation jumps suddenly. Fig. 5.9 (b) shows the stress of a finite element in a silicon indentation simulation from the previous chapter. Again the arrow marks the point just before the phase transformation occurs: the change in the stress of the finite element is dramatic. This jump in the microscopic stress is manifested on the macroscopic level as bumps in the simulated load vs. displacement curve shown in Fig. 4.1 (a) (this is not simply an artifact of the simulation: there is also a bump in the experimental curve. Fig. 4.1 (b). but only during unloading). This is a nice illustration of how differences in the microscopic energy surface of silicon and $PbTiO_3$ give rise to different macroscopic behavior.

5.5 Discussion

We came across some interesting physics in our examination of $PbTiO_3$. We have been able to connect the microscopic softening of phonons with asymmetric macroscopic response to strong electric fields. We discovered a completely unexpected inverted macroscopic hysteresis effect. Finally, the observation that switching occurred smoothly in the absence of an external electric field. and that the finite elements never switched through or to a tetragonal phase is important not only because it implies that the microscopic physical behavior of the system is different from what was expected. but also because it suggests that the present micromechanical modeling schemes based on sudden switching between tetragonal phases may not always be sufficient or justified.

We can also make several comments about experiments. The asymmetry in the load with respect to electric field direction should be observable for large electric fields, even at small indentation depths. The simulations were for a single crystal. but the effect should also be observable for poled polycrystalline samples. The observation of continuous switching in the absence of an electric field indicates that in experiments it will be difficult to probe the onset of switching behavior via indentation, which simulation suggests should occur at indentation depths around $0.02r_I$. The combination of strong elastic coupling between neighboring regions and small atomic displacements during polarization switching results in smooth macroscopic behavior. In contrast, the macroscopic measurements of silicon during indentation are able to provide information about the onset of phase transformations (see Refs. [1, 9, 11] for example). Finally, detecting the inverted macroscopic hysteresis loop in the load vs. displacement curve will be challenging, since conventional plastic deformation evident in Fig. 5.1(b) will tend to wash out the inverted hysteresis effect. Detecting the presence of non-reversibility in the system due to switching may be better probed by studying the polarization of the sample (see Fig. 5.3(d)).

Chapter 6

Summary and Conclusions

We began this thesis with a few simple questions about a spring, in order to illustrate that even for the simplest systems it is exceedingly difficult to predict how changes on the atomic scale affect mechanical behavior on the macroscopic scale. Changes on the atomic scale can influence how structures over a wide range of length scales interact with and affect one another, and it is daunting to try to disentangle how these various structures ultimately give rise to observed macroscopic behavior. However, the endeavor is both philosophically compelling and potentially exceedingly useful. So despite the difficulties of the problems faced, multiscale modelling is an active area of research.

The work described in the previous chapters is a tiny part of this larger endeavor, though perhaps our emphasis here is slightly different than other work done in the field. Our simulation technique, the quasicontinuum method extended to handle complex Bravais lattices, is relatively simple and straight-forward to implement. It is designed to model a certain type of physical system, of which indentation of complex materials is one example. In a natural way our method models some of the important physics of such a system: the rapidly varying strain fields caused by the indenter, strong elastic coupling between neighboring regions of the material, and a local energy surface that broadly captures the complexity of the true local energy surface. We had a few central questions in our mind during the study. Which results from our method are robust. and which are dependent on details of the finite element mesh or flaws in the underlying atomic potential? Given the (incomplete) list of physics incorporated into our method. what can we learn about the fundamental behavior of the systems we study? Finally, can we connect with experiment?

6.1 Silicon Indentation

Silicon indentation has received a great deal of attention since experimentalists found indications of a reversible phase transformation occurring underneath the indenter. Subsequent experimental work discovered a variety of curious behaviors, including hysteretic or discontinuous macroscopic measurements. Computational studies have been frustrated by the multiscale nature of the system, and have not been able to reproduce any of the unusual macroscopic behavior found in experiments.

In applying our computational method to silicon indentation, we first explored the robustness of simulation results with respect to changes in potential and finite element mesh parameters. We found that macroscopic curves and the geometry of the transformed region appear robust, but certain microscopic details such as the types of phases that form underneath the indenter are not.

Focusing in on simulation results that appear robust, we made a variety of observations about the system. We found that the symmetry of the underlying crystalline lattice affects the geometry of the transformed region, and that the transformed region tends to be contiguous during loading, but tends to fragment upon unloading. We found indications that the energy surface of the system as a whole is degenerate. On the macroscopic level we produced simulated load vs. displacement and load vs. resistance curves that qualitatively reproduce available experimental data. The latter were produced with the aid of a model that links information about the geometry of transformed region with macroscopic resistance: its success validates a simple physical picture of the system's electrical resistance. We also proposed additional resistance measurements that would help clarify the nature of the reverse transformation in some experiments.

Though we hope to have contributed to the the understanding of this system, there are still a variety of unanswered questions. For example: How does cracking observed in experiments affect macroscopic curves? How does indenter geometry affect results? Finally, how does the generation of cracks and defects affect the microscopic behavior of the system?

6.2 Indentation of $PbTiO_3$

Lead titanate ($PbTiO_3$) is a piezoelectric, an important class of materials from a technological point of view. Unfortunately there is not the experimental guidance for indentation of $PbTiO_3$ that there is for silicon. We compared our simulation results with experiment where possible, but our principal focus was to explore the physics of piezoelectric indentation. We paid particular attention to the connection between the microscopic features of the energy surface, and the macroscopic results.

We were able to link the asymmetry observed in simulated load vs. displacement curves with respect to electric field direction with the asymmetry of certain phonon frequencies with respect to that same field. This asymmetry in the load vs. displacement curve should be observable in experiments. We also noted that in the absence of external electric fields, the polarization of individual finite elements evolves continuously and takes unexpected paths through phase space, calling into question some theoretical models of piezoelectric switching. This behavior was attributed to details of the energy surface and the strong elastic coupling between neighboring regions of the material.

In the presence of large electric fields, discontinuous switching is observed, but all macroscopic measurements remain smooth. This behavior is very different from silicon, and for $PbTiO_3$ makes the prospect of a finding a macroscopic signature for microscopic switching doubtful. For particular orientations of the electric field, we observed a reverse hysteresis loop in the load vs. displacement curve, where at a given indentation depth the load is *higher* during unloading than during loading. This effect, which results from the external electric field doing work on the piezoelectric during indentation, is unexpected and counter-intuitive. Unfortunately, it would be very difficult to observe in experiments since permanent deformation due to plastic effects would tend to wash the effect out.

Further experimental work would be useful for guiding future computational work. But even without additional guidance some unresolved issues are particularly intriguing: How does the polycrystalline nature of most piezoelectric samples affect indentation results? Would a more accurately modelled electric field affect results substantially? Finally, how does the generation of cracks and defects affect switching behavior?

6.3 Future Directions

We hope we have contributed to the understanding of indentation of silicon and $PbTiO_3$. Further progress requires making some improvements to our simulation technique, though most of the improvements would be quite involved. Since our method is based on atomistic potentials, improvements in them will increase the utility and accuracy of our results. The role of cracks and defects in the systems we studied is not well understood, and modelling these features somehow would be very useful. Incorporating finite temperature, especially for the case of silicon, would also be helpful.

There are a few improvements to the method that would be particularly useful for modelling $PbTiO_3$ and other piezoelectrics. First, modelling a specific realization of a polycrystal should be straight-forward. This would help us understand how having a collection of grains affects the microscopic behavior of the system, and would also enable us to make a closer connection with experiment. Second, we would like to treat the electric field more accurately. Currently the electric field is constant throughout the system, which is not realistic. Correctly taking into account the contribution due to the nonuniform polarization of the system would enable us to explore how electric interactions between nearby regions affect the system's behavior. Also, there would be additional theoretical and experimental results that we could check our results against. Changes in the polarization of the sample as indentation proceeds causes changes in the surface charge, which has been calculated and experimentally measured (via velocity vs. current through the indenter curves) by Ramamurty *et al.* [4].

Of course, there are other potential applications that go beyond indentation of silicon and $PbTiO_3$. Martensitic transformations in metals in response to strain fields are one possibility. Other potential applications are in the technologically important field of thin film piezoelectrics. These materials do not behave as bulk piezoelectrics, and there are many open questions about how finite size effects, grain sizes, and polarization orientation affect performance.

Bibliography

[1] E. R. Weppelmann. J. S. Field. and M. V. Swain. J. Mater. Res. **8**. 830 (1993).

[2] G. M. Pharr, W. C. Oliver, and D. R. Clarke, J. of Elec. Mat. **19**. 881 (1990).

[3] G. M. Pharr *et al.*, J. Mater. Res. **7**, 961 (1992).

[4] U. Ramamurty, S. Sridhar, A. E. Giannokopoulos, and S. Suresh. Acta Mater. **47**, 2417 (1999).

[5] E. B. Tadmor, M. Ortiz, and R. Phillips, Phil. Mag. A **73**, 1529 (1996).

[6] E. B. Tadmor, G. S. Smith, N. Bernstein, and E. Kaxiras, Phys. Rev. B **59**, 235 (1999).

[7] N. C. MacDonald. in *Nanotechnology*, edited by G. Timp (Springer-Verlag, New York, 1999).

[8] D. R. Clarke, M. C. Kroll, P. D. Kircher, and R. F. Cook, Phys. Rev. Lett. **60**. 2156 (1988).

[9] E. R. Weppelmann, J. S. Field, and M. V. Swain, J. Mater. Sci. **30**, 2455 (1995).

[10] A. Kailer and Y. G. G. an K. G. Nickel, J. Appl. Phys. **81**, 3057 (1997).

[11] A. B. Mann, D. van Heerden, J. B. Pethica, and T. P. Weihs, submitted to J. Mater. Res .

[12] J. S. Williams. Y. Chen. J. Wong-Leung, and A. Kerr. J. Mater. Res. **14**, 2338 (1999).

[13] A. F. Devonshire, Phil. Mag. Suppl. **3**, 85 (1954).

[14] H. Cao and A. G. Evans, J. Am. Ceram. Soc. **76**, 890 (1993).

[15] O. Auciello, J. F. Scott, and R. Ramesh, Physics Today **51**, 22 (1998).

[16] F. D. Fischer and E. Werner, Z. angew. Math. Mech. **77**, 341 (1997).

[17] L. E. Tanner, D. Schryvers, and S. M. Shapiro, Mater. Sci. Eng. A **127**, 205 (1990).

[18] D. Schryvers, habilitation, University of Brussels (1991).

[19] L. Xiadong and B. Bhushan, Thin Solid Films **340**, 210 (1999).

[20] W. C. Oliver and C. J. McHargue, Thin Solid Films **161**, 117 (1999).

[21] D. F. Bahr *et al.*, Mat. Sci. Eng. A **259**, 126 (1999).

[22] J. S. Kallman *et al.*, Phys. Rev. B **47**, 7705 (1993).

[23] R. Pérez, M. C. Payne, and A. D. Simpson, Phys. Rev. Lett. **75**, 4748 (1995).

[24] A. K. Bhattacharya and W. D. Nix, Int. J. Solids Struct. **24**, 881 (1988).

[25] J. A. Knapp *et al.*, J. Appl. Phys. **85**, 1460 (1999).

[26] A. E. Giannokopoulos and S. Suresh, Acta Mater. **47**, 2153 (1999).

[27] J. E. Marsden and T. J. R. Hughes, in *Mathematical Foundations of Elasticity* (Dover Publications, New York, 1983), Chap. 3.

[28] T. J. R. Hughes, *The Finite Element Method* (Prentice-Hall, Englewood Cliffs, 1987).

[29] M. Papadrakakis and P. Ghionis, Comp. Meth. Appl. Mech. Eng. **59**, 11 (1986).

[30] F. Milstein, in *Mechanics of Solids*, edited by H. G. Hopkins and M. J. Sewell (Pergamon Press, New York, 1982).

[31] V. B. Shenoy *et al.*, J. Mech. Phys. Sol. **47**, 611 (1999).

[32] J. W. Martin, J. Phys. C **8**, 2858 (1975).

[33] J. W. Martin, J. Phys. C **8**, 2837 (1975).

[34] C. S. G. Cousins, J. Phys. C **11**, 4867 (1978).

[35] R. O. Jones and O. Gunnarsson, Rev. Mod. Phys. **61**, 689 (1989).

[36] M. C. Payne *et al.*, Rev. Mod. Phys. **64**, 1045 (1992).

[37] F. H. Stillinger and T. A. Weber, Phys. Rev. B **31**, 5262 (1985).

[38] N. Bernstein and E. Kaxiras, Phys. Rev. B **56**, 10488 (1997).

[39] U. V. Waghmare and K. M. Rabe, Phys. Rev. B **55**, 6161 (1997).

[40] A. D. Vita, Ph.D. thesis, Keele University (1992).

[41] A. Z. Sommerfeld, Z. Phys. **47**, 1 (1928).

[42] H. Hellman, *Einfrüngen in die Quantenchemie* (Deuticke, Leipzig, 1937).

[43] R. P. Feynman, Phys. Rev. **56**, 340 (1939).

[44] L. D. Landau and E. M. Lifshitz, *Statistical Physics* (Pergamon Press, New York, 1963).

[45] L. L. Boyer *et al.*, Phys. Rev. Lett. **67**, 715 (1991).

[46] C. L. Kelcher, S. J. Plimpton, and J. C. Hamilton, Phys. Rev. B **58**, 11085 (1998).

[47] H. Hertz, J. Reine angewandte Mathematik **92**, 156 (1882).

[48] R. Holm, *Electric Contacts: Theory and Application* (Springer-Verlag, New York, 1967).

[49] H. Wang and R. N. Singh, J. Appl. Phys. **81**, 7471 (1997).

[50] D. Vanderbilt. Curr. Op. Solid State Mat. Sci. **2**. 701 (1997).

[51] W. Lu. D.-N. Fang, C. Q. Li, and K.-C. Hwang, Acta Mater. **47**. 2913 (1999).

[52] X. Chen, D.-N. Fang, and K.-C. Hwang, Acta Mater. **45**, 3181 (1996).

[53] E. B. Tadmor. U. V. Waghmare. G. S. Smith, and E. Kaxiras. unpublished .